Ocean Engineering 326 (2025) 120871

Contents lists available at ScienceDirect

Ocean Engineering

journal homepage: www.elsevier.com/locate/oceaneng

Research paper

A deep modal model for reconstructing the VIV response of a flexible cylinder with sparse sensing data

Yangyang Liao, Hesheng Tang *, Liyu Xie

Department of Disaster Mitigation for Structures, College of Civil Engineering, Tongji University, Shanghai, 200092, China

ARTICLE INFO

Keywords:
Vortex-induced vibration
Flexible cylinder
Deep modal model
Sparse sensing data
Displacement reconstruction

ABSTRACT

In the field of civil and ocean engineering, due to the limitations of sensor placement and the complexity of large-scale structures, obtaining continuous and comprehensive monitoring data is often highly challenging. To address this issue, this paper proposes a deep modal model for reconstructing the vortex-induced vibration (VIV) response of a flexible cylinder using sparse sensing data. A pre-trained model is first used to extract the modal characteristics of the flexible cylinder; a long short-term memory (LSTM) model is then employed to represent the modal weight functions. The pre-trained modal model is transferred as implicit physical laws into the LSTM model to reconstruct the global displacement of the flexible cylinder. The effectiveness of the proposed deep modal model is validated through a numerical case study involving a top-tensioned riser. On this basis, displacement fields of a smooth cylinder and cylinders with 3 or 4 control rods are reconstructed using sparse sensor data from seven locations in the experiment. The proposed deep modal model can be applied to reconstruct structural displacement fields, identify structural damage, and optimize sensor placement, offering significant benefits for structural health monitoring.

1. Introduction

In the field of modern civil and ocean engineering, as the scale and complexity of structures increase, real-time monitoring and assessment of structural conditions have become particularly important (Li et al., 2016; Wang et al., 2018). Structural health monitoring (SHM) technology offers an effective means for early detection of potential structural damage and disaster prevention (Wang et al., 2024). With the rapid development of sensor technology, various types of monitoring devices have been proposed and applied across different engineering fields (Jiang et al., 2024; Li et al., 2024; Xue et al., 2024). However, due to the large size and complex shapes of structures in real engineering projects, sensor placement is often constrained by factors such as physical space, installation difficulty, and cost, making it challenging to achieve dense sensor deployment across the entire structure (Sun and Büyüköztürk, 2015). This limitation often results in incomplete data, hindering comprehensive and accurate assessments of the structural condition, and thereby increasing the difficulty of predicting structural damage and fatigue. This is especially true for large-scale marine structures such as flexible risers and platforms, where obtaining comprehensive vibration data becomes more complex and challenging (Du et al., 2024). Therefore, how to utilize sparse sensor data to achieve full-field displacement reconstruction, while ensuring monitoring accuracy, has become a critical research direction in the current field of structural health monitoring.

The vortex-induced vibration (VIV) caused by vortex shedding is one of the most typical fluid-structure interaction (FSI) phenomena in the field of fluid mechanics (Zhang et al., 2024). VIV not only poses a threat to the stability of structures but also accelerates their fatigue damage, potentially leading to catastrophic accidents. Over the past 100 years, scholars from both academia and industry have conducted extensive research on the response characteristics of VIV in pipelines, aiming to explore its underlying mechanisms and to find effective control strategies (Zhu et al., 2024; Liu et al., 2024; Duranay et al., 2023). Esmaeili and Rabiee (2021) investigated the effectiveness of using an active control system, specifically a time delay estimation based intelligent proportional-integral-derivative (TDE-iPID) controller, to reduce flow-induced vibrations around a sprung cylinder. Xu et al. (2020) experimentally investigated the response characteristics of side-by-side flexible cylinders with and without helical strakes in a towed tank. Martini et al. (2021) presented numerical simulations of flow around an elastically-mounted circular cylinder with one degree of freedom

* Corresponding author.
E-mail address: thstj@tongji.edu.cn (H. Tang).

https://doi.org/10.1016/j.oceaneng.2025.120871
Received 23 September 2024; Received in revised form 1 February 2025; Accepted 2 March 2025
Available online 9 March 2025

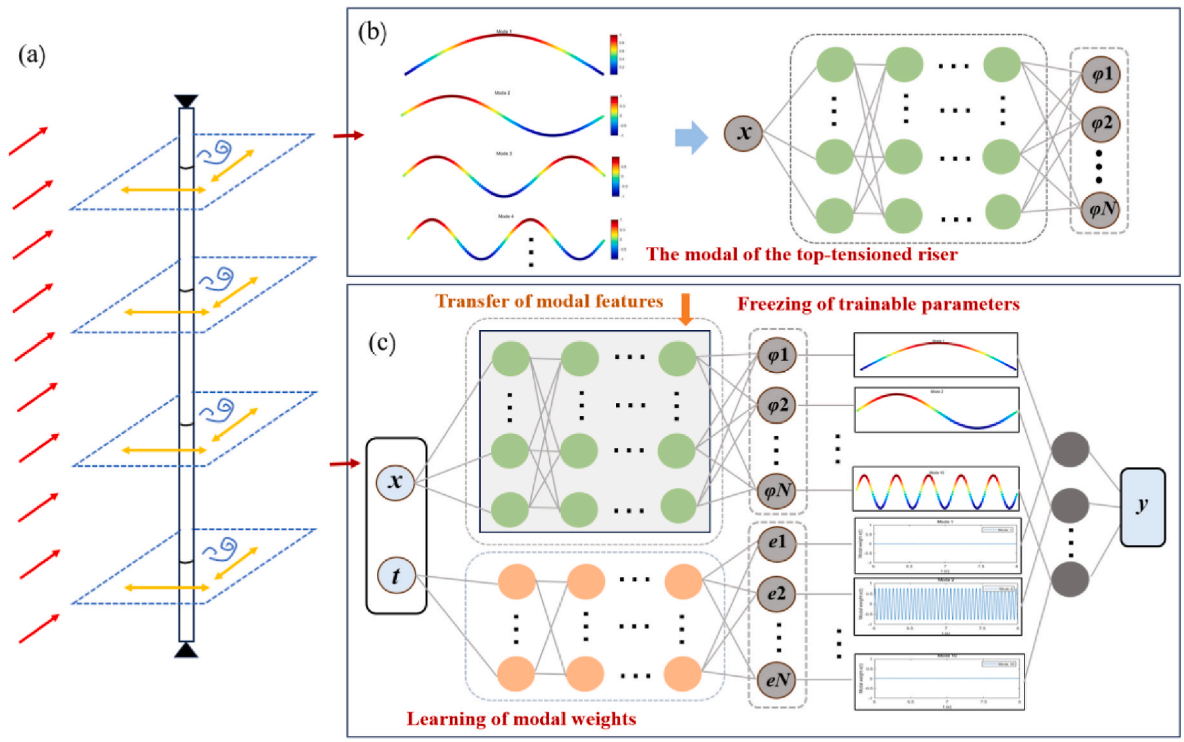

Fig. 1. The schematic of deep modal model. (a) VIV of the flexible riser; (b) Learning of different modal features of the flexible riser; (c) Learning of the modal weights.

(1-DOF), showing that a 2D approach is effective for the lower branch, while significant discrepancies arise in the upper branch. These spatio-temporal data resources, derived from experiments, monitoring, or simulations, contain vast amounts of hidden information and physical knowledge. Valuable insights can be extracted from this data to assist humans and systems in making more effective decisions and conducting state analysis (Amato et al., 2020).

In fact, dataset is the concrete manifestation of natural physical laws and the discretized form of function mappings for various physical variables. The basic idea of traditional data-driven deep learning (DL) is to use algorithms to analyze data, learn features from the data, and understand these features, then make decisions or predictions about real-world events (Liu et al., 2023). Due to their powerful nonlinear fitting capabilities, DL models can provide efficient and precise prediction results under sufficient discrete data conditions, and have been widely applied across various fields (Kamilaris and Prenafeta-Boldú, 2018; Lake and Baroni, 2023). An approach, proposed by Sekar et al. (2019), combined deep convolutional neural networks (CNN) and deep multilayer perceptrons (MLP) to quickly predict the incompressible laminar steady flow field based on airfoil geometry, Reynolds number, and angle of attack. Fukami et al. (2019) developed CNN and hybrid downsampled skip-connection/multi-scale (DSC/MS) models to perform super-resolution analysis, successfully reconstructing high-resolution laminar and turbulent flow fields from low-resolution data with remarkable accuracy, demonstrating potential for revealing subgrid-scale physics in complex turbulent flows. Brener et al. (2024) developed a data-driven machine learning turbulence model using the Reynolds force vector (RFV) as the target for ML techniques, demonstrating lower error propagation and enhanced accuracy in Reynolds-averaged Navier–Stokes (RANS) simulations compared to other approaches. However, how to integrate physical laws with the data distribution space to reduce the dependency of DL models on data, and further improve prediction accuracy and generalization ability, remains a challenge in current research (Raissi et al., 2019; Weber et al., 2023).

To date, experimental research remains one of the most effective methods for understanding the problem of VIV, offering reliable data and intuitive observations. Experimental studies are generally divided into two forms: in-situ tests and model experiments (Zhang et al., 2020; Mukundan et al., 2009). Jiang et al. (2021) conducted an experimental study on the VIV of two side-by-side risers in uniform flow, analyzing the effects of varying structural and hydrodynamic parameters, such as flow velocity and spacing ratio, on the dynamic feedback between a smooth riser and a riser equipped with triple helical strakes. Zhu et al. (2021) experimentally investigated the VIV of a catenary flexible riser in log-law sheared flows, using nonintrusive imaging to capture in-plane and out-of-plane responses, and found asynchronous mode transitions and spatial variation in dominant frequencies along the span. Gao et al. (2015) conducted an experimental investigation on a flexible riser with and without various helical strake configurations to analyze the VIV response performance under uniform and linearly sheared flows, focusing on displacement responses and fatigue damage. However, whether dealing with full-scale structures or scaled models, experiments are often constrained by costs and monitoring technologies, resulting in data that is discrete and sparse. This poses significant challenges for the application of traditional data-driven DL models (Karniadakis et al., 2021): 1) a lack of sufficient training samples to maintain the model's generalization ability and high performance; 2) data-driven DL only fits the data space without incorporating physical relevance. Moreover, since VIV responses involve complex FSI processes and the system's dynamic characteristics are highly nonlinear, traditional DL models have certain limitations in capturing and predicting the full-field vibration behavior of structures.

Based on this, this paper proposes a deep modal model that combines modal analysis with a long short-term memory (LSTM) network to achieve high-precision reconstruction of the global VIV response of flexible cylindrical structures using sparsely placed sensor data. First, the method uses a data-driven DL model to extract different order modal features of the structure; the pre-trained modal features are then transferred to the LSTM model. Based on the sparse sensor data, the

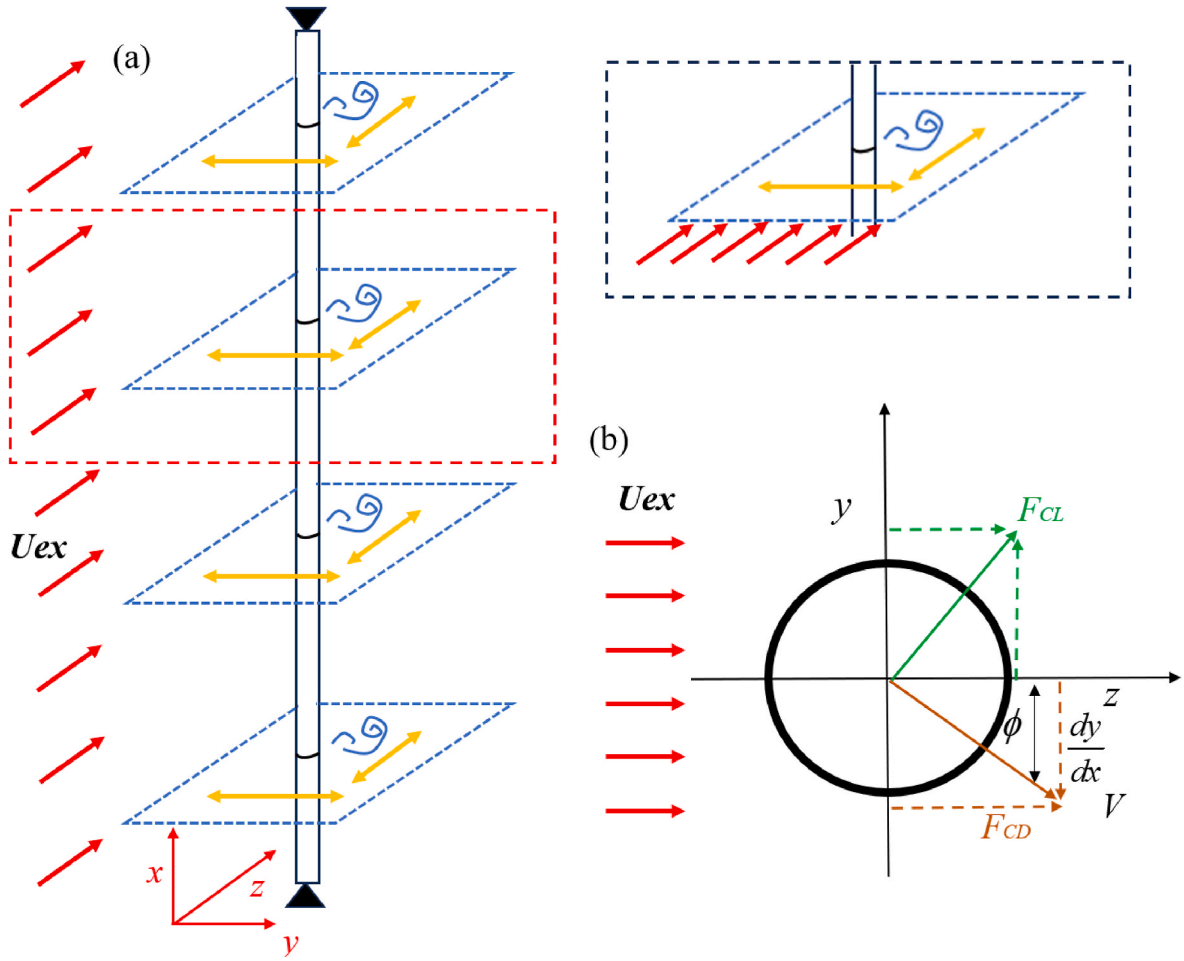

Fig. 2. Hydrodynamic model of the top-tensioned riser. (a) VIV of the flexible riser; (b) Force diagram of the riser.

Table 1
The parameters used in the numerical case study.

No.	Parameters	Value
1	Length of riser	9.63 m
2	Outer diameter of riser	20 mm
3	Inner diameter of riser	19.1 mm
4	Mass of riser	0.586 kg/m
5	Bending stiffness EI	135.4 Nm^2
6	Top-end tension F_{top}	817 N
7	External flow velocity U_{ex}	0.42 m/s

Table 2
The independency study of the spatial steps.

No.	Space step ($\Delta\tau = 0.001$)	$\eta_{rms,\xi=0.2}$	Dominant frequency
1	10	0.517194	3.214
2	50	0.521813	3.285
3	100	0.521357	3.285
4	200	0.535819	3.285
5	400	0.539133	3.285

LSTM model is used to learn the time-varying characteristics of the weight functions of different order modes. On this basis, the global displacement field of the structure is reconstructed. The structure and main contents of this paper are as follows: In Section 2, the fundamental structure and principle of the deep modal model are provided. In Section 3, the reliability of the deep modal model is validated by using a numerical case study of the top-tensioned riser. In Section 4, the deep modal model is applied to reconstruct the displacement fields of a smooth cylinder and cylinders with 3 or 4 control rods by using sparse sensor data from 7 locations in the experiment. Finally, the primary conclusions of this paper are presented in Section 5.

2. The schematic of deep modal model

For the flexible cylinder system, its vibration response can be characterized as the superposition of modal shapes of different orders $\phi_i(x)$ ($i = 1, 2, 3, \ldots$), that is (Lie and Kaasen, 2006; Trim et al., 2005):

$$y(x,t) = \sum_{i=1}^{N} e_i(t)\phi_i(x) \tag{1}$$

Where $\phi_i(x)$ represents different orders mode-shapes, and $e_i(t)$ represents the modal weight, N represents the number of modes, $y(x,t)$ is the displacement response. The mode shapes are inherent characteristics of the structure, depending solely on the properties of the structural system and are independent of external excitations. Typically, the mode shapes of a structure can be obtained through analytical methods, finite element methods (FEM), or experiments.

Based on this, a deep modal model for the reconstruction of the displacement field of the flexible riser is developed, as shown in Fig. 1. The construction of this model mainly involves two steps.

(1) *Characterization of normalized modal shapes based on deep learning.* First, the modal shapes are obtained based on analytical methods or FEM, combined with the inherent properties of the riser. A

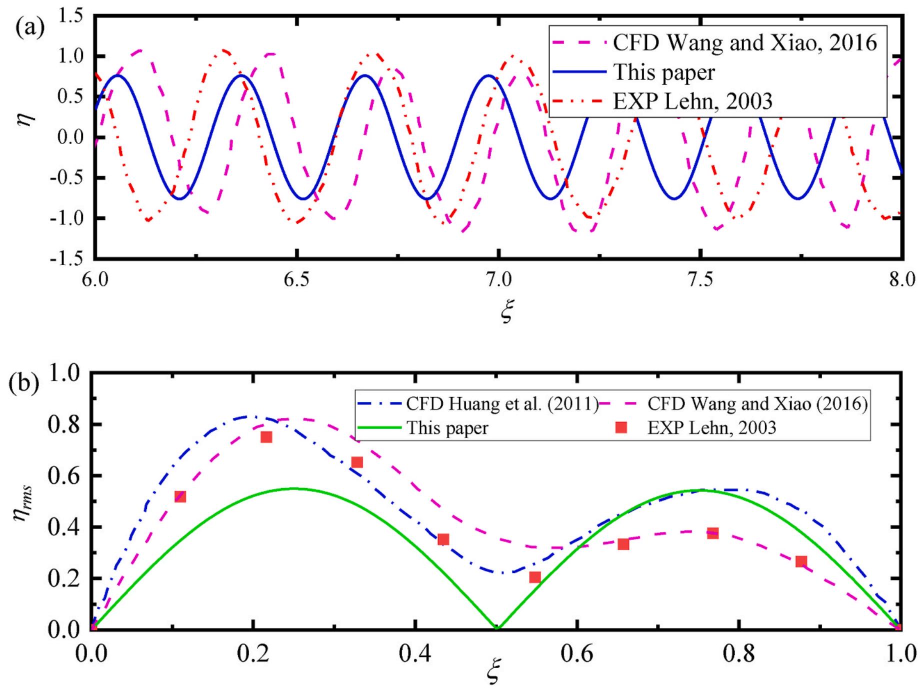

Fig. 3. The computational results compared with CFD results and experimental results ($x/L = 0.22$). (a) CFD results (Wang and Xiao, 2016; Huang et al., 2011); (b) Experimental results (Lehn, 2003).

deep learning model is then used to establish the mapping relationship between the spatial coordinates x and the modal shapes of different orders $\widehat{\phi}_i(x)$ $(i = 1, 2, 3, \ldots)$. The full connected neural network (FCNN) model is used in this paper.

(2) *Learning of modal weights.* The deep learning model (such as DNN, LSTM, etc.) is used to establish the mapping relationship between time t and the corresponding modal weights of different orders $\widehat{e}_i(t)$ $(i = 1, 2, 3, \ldots)$. The LSTM model is used in this paper. The trained DL model $\widehat{\phi}_i(x)$ $(i = 1, 2, 3, \ldots)$ with modal features is transferred to the LSTM model $\widehat{e}_i(t)$ $(i = 1, 2, 3, \ldots)$ architecture, where the parameters are set to a non-trainable state (frozen). The modal weights are multiplied by the corresponding modal shapes and summed to output the displacement response of the riser $\widehat{y}(x) = \sum_{i=1}^{N} \widehat{e}_i(t)\widehat{\phi}_i(x)$. The entire model is trained using spatially sparse observational data. Based on this, the displacement response of the structure at all positions can be obtained using vibration response data collected by spatially sparsely distributed sensors.

Compared with traditional modal analysis methods, the deep modal model utilizes a sub-network to extract physical features from discrete mode shapes that cannot be expressed by functions. Combined with FEM and experiments, it is applicable to various complex boundaries and structures. Furthermore, the embedding and transfer of modal features can effectively enhance the interpretability, generalization, and efficiency of traditional deep learning models. Through the transfer of modal characteristics, the deep modal model can be generally applied to similar structures and serves as a reliable tool for analyzing structural vibration.

3. Model validation based on numerical results

To validate the effectiveness of the constructed deep modal model, this section presents a numerical case study of a top-tensioned riser. Using the vibration response time history data from spatially sparse locations, the displacement at all positions along the top-tensioned riser is reconstructed.

3.1. The numerical model and modal analysis

3.1.1. The numerical model

The cross-sectional force analysis is conducted on the top-tensioned riser, as show in Fig. 2. By considering the added mass term, the force exerted on the circular cross-section in the y-direction (cross-flow direction, CF) can be expressed as (Gao et al., 2018):

$$\begin{aligned} F_{ex} &= F_{CL}\cos\phi - F_{CD}\sin\phi - m_a\frac{d^2y}{dt^2} \\ &= \frac{1}{2}\rho_{ex}D_{ex}\sqrt{U_{ex}^2 + \left(\frac{dy}{dt}\right)^2}\left(C_L U_{ex} - C_D\frac{dy}{dt}\right) - m_a\frac{d^2y}{dt^2} \end{aligned} \tag{2}$$

Where ϕ is the angle between the instantaneous incoming flow velocity V and the external flow velocity U_{ex}, F_{CL} and F_{CD} are the lift force and drag force acting on the riser, C_L and C_D are the lift coefficient and drag coefficient, F_{ex} is the resultant force in the y-axis, y is the displacement of the riser in the y-axis, t is time, m_a is the added mass per unit length, and ρ_{ex} is the density of the external fluid. According to the geometric relationship, $\sin\phi = \frac{dy/dt}{\sqrt{U_{ex}^2+(dy/dt)^2}}$, $\cos\phi = \frac{U_{ex}}{\sqrt{U_{ex}^2+(dy/dt)^2}}$. For the drag coefficient C_D in the subcritical region ($300 \le \mathrm{Re} \le 3\times 10^5$), its value is taken as 1.2 (Blevins, 1977).

According to the Morison equation, the added mass m_a of a cylindrical structure can be expressed as:

$$m_a = \frac{1}{4}C_a\pi\rho_{ex}D_{ex} \tag{3}$$

Where D_{ex} is the diameter of the cylinder, and C_a is the added mass coefficient, which is taken as 1.0 for circular structures.

Building on this, the lift coefficient is modeled using an acceleration-coupled van der Pol wake oscillator (Facchinetti et al., 2004), which can be expressed as:

$$C_L = \frac{1}{2}C_{L0}q \tag{4a}$$

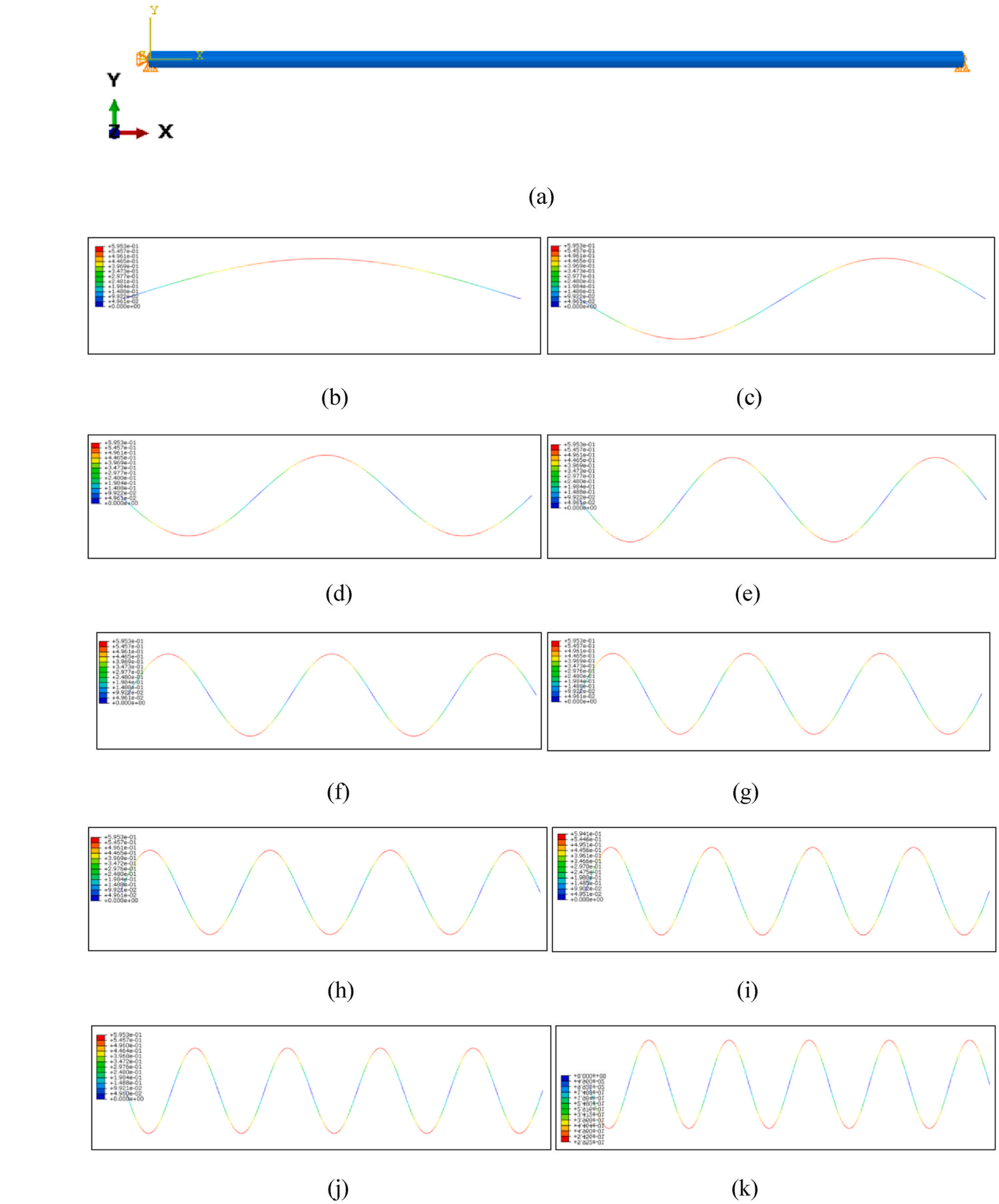

Fig. 4. Finite element model and corresponding mode shapes. (a) Finite element model; (b)–(k) The first 10 mode shapes.

$$\frac{d^2q}{dt^2}+\varepsilon_w\omega_s\left(q^2-1\right)\frac{dq}{dt}+\omega_s^2q=\frac{S_w}{D_{ex}}\frac{d^2y}{dt^2} \tag{4b}$$

Where C_{L0} is the lift coefficient when the cylinder is stationary, and in the subcritical region, its value is taken as 0.3. q is the dimensionless vortex-induced lift coefficient. ε_w and S_w are empirical parameters, taken as 0.3 and 1.2, respectively (Facchinetti et al., 2004). The circular frequency of vortex shedding ω_s can be expressed as:

$$\omega_s=2\pi St\frac{U_{ex}}{D_{ex}} \tag{5}$$

When vortex-induced vibration occurs in the cylinder, the Strouhal number St is approximately 0.17 (Chaplin et al., 2005).

Therefore, the force exerted on a specific cross-section of the top-

Table 3
The parameters used in the numerical case study.

Mode	FEM (Hz)	Theoretical Value (Hz)	Error
1	0.2575	0.2573	0.078%
2	1.0299	1.0291	0.078%
3	2.3172	2.3155	0.073%
4	4.1194	4.1165	0.070%
5	6.4364	6.4320	0.068%
6	9.2681	9.2621	0.065%
7	12.615	12.606	0.071%
8	16.475	16.466	0.055%
9	20.851	20.840	0.053%
10	25.741	25.728	0.051%

tensioned riser can be expressed as:

$$\begin{cases} F_{ex} = \dfrac{1}{2}\rho_{ex} D_{ex}\sqrt{U_{ex}^2 + \left(\dfrac{dy}{dt}\right)^2}\left[\dfrac{1}{2}C_{L0}U_{ex}q - C_D\dfrac{dy}{dt}\right] - \dfrac{1}{4}C_a\pi\rho_{ex}D_{ex}^2\dfrac{d^2y}{dt^2} \\ \dfrac{d^2q}{dt^2} + \varepsilon_w\omega_s\left(q^2-1\right)\dfrac{dq}{dt} + \omega_s^2 q = \dfrac{S_w}{D_{ex}}\dfrac{d^2y}{dt^2} \end{cases} \tag{6}$$

The top-tensioned riser can be regarded as the Euler-Bernoulli beam, and its equation under external loading can be expressed as (as shown in Fig. 2):

$$m_s\frac{\partial^2 y}{\partial t^2} + c\frac{\partial y}{\partial t} - \frac{\partial}{\partial x}\left[F_T\frac{\partial y}{\partial x}\right] + EI\frac{\partial^4 y}{\partial t^4} = F_{ex} \tag{7}$$

Where m_s is the mass per unit length of the riser, c is the damping coefficient, EI is the bending stiffness, and F_T is the effective tension within the riser, which can be expressed as:

$$F_T = F_{top} + (A_{ex}\rho_{ex}g - m_s g)(L - x) \tag{8}$$

Where F_{top} is the top tension, A_{ex} is the cross-sectional area of the riser, g is the gravitational acceleration, taken as 9.8 m/s^2, and L is the total length of the riser. The damping coefficient includes the structural damping coefficient c_s and the fluid damping coefficient c_f:

$$c = c_s + c_f = c_s + \gamma\rho_{ex}\Omega_f D_{ex}^2 \tag{9}$$

To achieve the maximum vibration of the structure, $c_s = 0$, where Ω_f represents the vortex shedding frequency, and γ is the viscous force coefficient, which can be obtained from the following equation:

$$\Omega_f = \omega_s = 2\pi St U_{ex}/D_{ex} \tag{10}$$

$$\gamma = C_D/(4\pi St) \tag{11}$$

Therefore, after the non-dimensionalization process, the vibration equation for the VIV of a flexible cylinder can be expressed as:

$$\begin{cases} (1 + C_a\beta_{ex})\dfrac{\partial^2\eta}{\partial\tau^2} + c^*\dfrac{\partial\eta}{\partial\tau} + \gamma\dfrac{\partial\eta}{\partial\xi} - F_{top}^*\dfrac{\partial^2\eta}{\partial\xi^2} + \dfrac{\partial^4\eta}{\partial\xi^4} = \dfrac{\beta_{ex}}{\pi}\sqrt{\nu_{ex}^2 + \left(\dfrac{\partial\eta}{\partial\tau}\right)^2}\left[C_{L0}\nu_{ex}q - 2C_D\dfrac{\partial\eta}{\partial\tau}\right] \\ \dfrac{\partial^2 q}{\partial\tau^2} + \varepsilon_w(2\pi St\nu_{ex})\left(q^2-1\right)\dfrac{\partial q}{\partial\tau} + (2\pi St\nu_{ex})^2 q = S_w\dfrac{\partial^2\eta}{\partial\tau^2} \end{cases} \tag{12}$$

Where $\eta = \frac{y}{D_{ex}}$, $\xi = \frac{x}{L}$, $\tau = \sqrt{\frac{EI}{m_s L^4}}t$, $\beta_{ex} = \frac{\pi\rho_{ex}D_{ex}^2}{4m_s}$, $c^* = \frac{cL^2}{\sqrt{m_s EI}}$, $\nu_{ex} = U_{ex}\sqrt{\frac{m_s L^4}{EID_{ex}^2}}$, $\gamma = \frac{(A_{ex}\rho_{ex} - m_s)gL^3}{EI}$, $F_{top}^* = \frac{\left[F_{top} - (A_{ex}\rho_{ex} - m_s)gL(1-\xi)\right]L^2}{EI}$.

The analyzed top-tensioned riser has a length of 9.63 m, an outer diameter of 20 mm, an inner diameter of 19.1 mm, a mass of 0.586 kg/m, a bending stiffness $EI = 135.4$ Nm^2, a top-end tension of 817 N, and an external flow velocity of $U_{ex} = 0.42$ m/s (as show in Table 1) (Lehn, 2003). The spatial domain is discretized using the finite difference

Table 4
Configuration of platform for model training.

Configuration	Performance indicators
System	Windows 11 64-bit
CPU	Intel® Core™ i9-14900K 3.20 GHz
GPU	NVIDIA GeForce RTX 4090 24G
RAM	64 G
CUDA	11.2
Python	3.8.19
Tensorflow	2.12.0

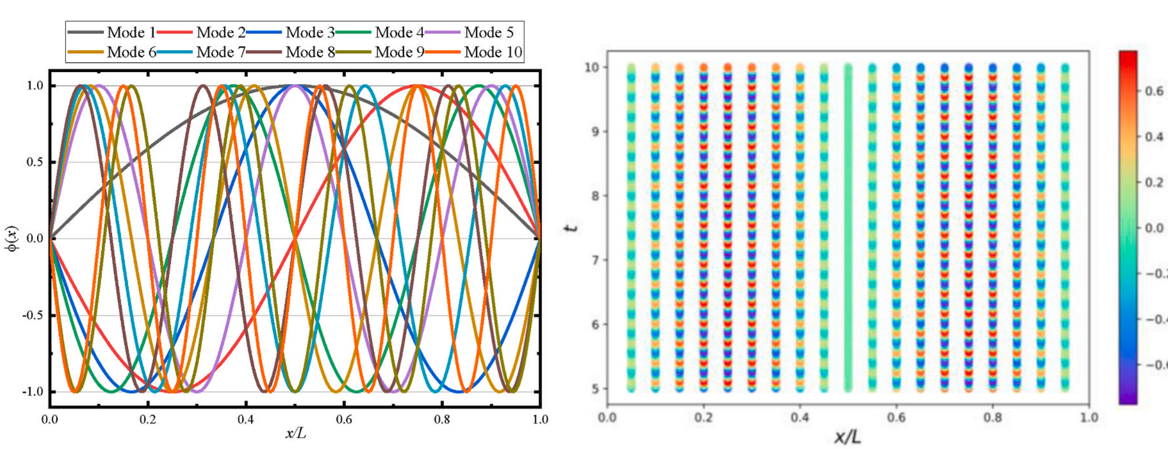

(a) (b)

Fig. 5. The training dataset of the numerical case. (a) Modal shape training data set; (b) Riser vibration response training data set.

Table 5
The hyperparameters specific to the model training.

Model	Architecture	Model architecture	Activation function	Optimizer	Learning rate	Initializer
Traditional DL	LSTM	4*256	Tanh/Sigmoid	Adamax	0.001	Glorot uniform
Deep modal model	FCNN	4*256	Sin	Adamax	0.0001	Glorot uniform
	LSTM	4*256	Tanh/Sigmoid		0.005	

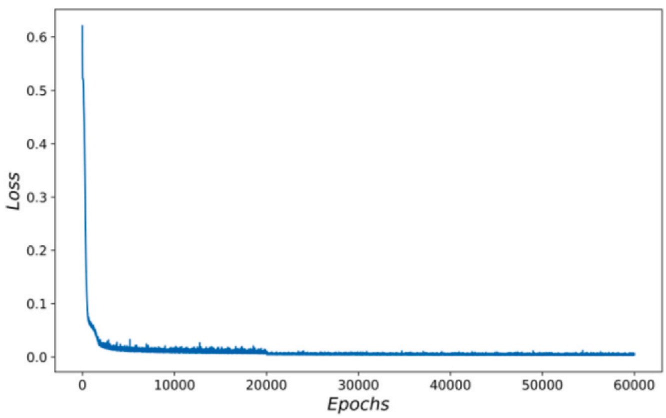

Fig. 6. Loss functions during pre-training process.

method (FDM), and the time domain is solved using the 4th-order Runge-Kutta method (4-RK).

To ensure the accuracy of the computational results, the MATLAB ode45 function is employed for time-domain solutions (i.e., adaptive time-stepping solutions), with the relative and absolute error tolerances set to 1E-6 and 1E-9, respectively. The solution is obtained at fixed time steps $\Delta\tau = 0.001$. Simultaneously, the independency study of the spatial steps is conducted. The displacement RMS values and dominant frequencies at $x/L = 0.2$ during $t = 6-20$ s are used as evaluation criteria, with the computational results presented in Table 2. Consequently, the riser is discretized into 201 points along the spatial domain (including the two end nodes). This process yields the time history response of the top-tensioned riser under uniform flow conditions. The computational results are compared with computational fluid dynamics (CFD) results (Wang and Xiao, 2016; Huang et al., 2011) and experimental results (Lehn, 2003) ($x/L = 0.22$), as shown in Fig. 3.

The calculation results presented in this paper, as shown in Fig. 3, exhibit some discrepancies compared to experimental measurements and CFD calculations. Specifically, the experimental and CFD methods indicate that the vibration displacement at the upper part of the riser is smaller, while the displacement at the lower part is larger. However, the displacement response calculated using the theoretical model in this paper is symmetric. This is due to the use of an acceleration-coupled van der Pol wake oscillator model to simulate vortex-induced forces, which is an approximate computational model. The added mass coefficient and drag coefficient are treated as constants, with values of $C_a = 1.0$ and $C_D = 1.2$. However, in the experimental and CFD methods, both the added mass and drag coefficients vary depending on the amplitude and frequency of the vibration of the riser. The same phenomenon was also observed in the study by Xie et al. (2019).

3.1.2. Modal analysis based on FEM

The first 10 mode shapes of the flexible cylindrical structure are analyzed based on the finite element method (FEM). A flexible cylinder model is established using two-dimensional beam elements, as shown in Fig. 4 (a), with the cylinder parameters listed in Table 1. The cylinder structure is discretized into 200 elements along its length. To ensure computational accuracy, the first 10 frequencies obtained from the FEM are compared with theoretical values, as presented in Table 3, with the maximum relative error being only 0.078%. The theoretical frequencies

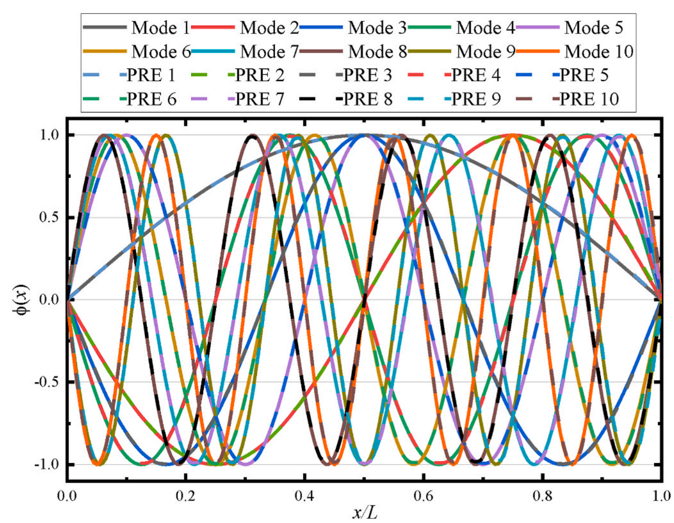

Fig. 8. Prediction results of normalized mode shapes by FCNN.

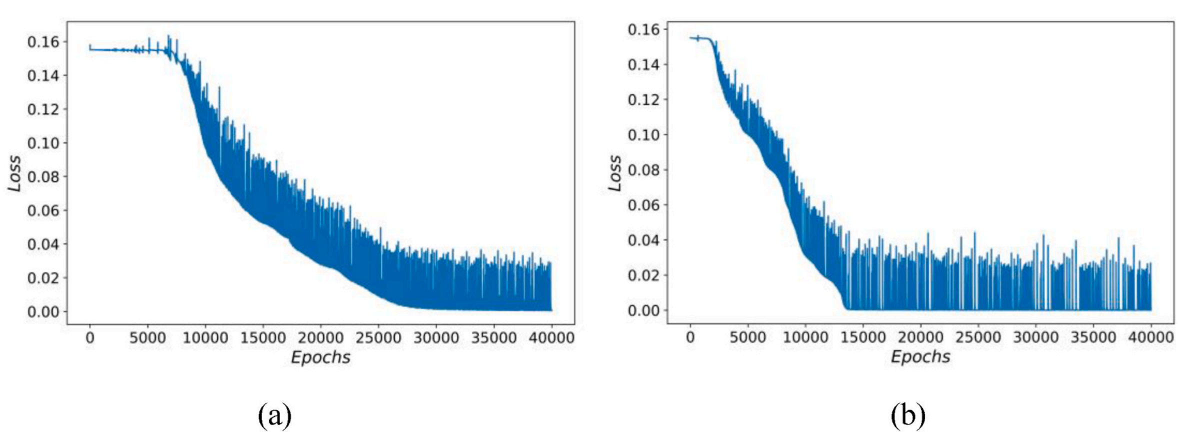

Fig. 7. Loss functions during the training process. (a) The traditional DL model; (b) The deep modal model.

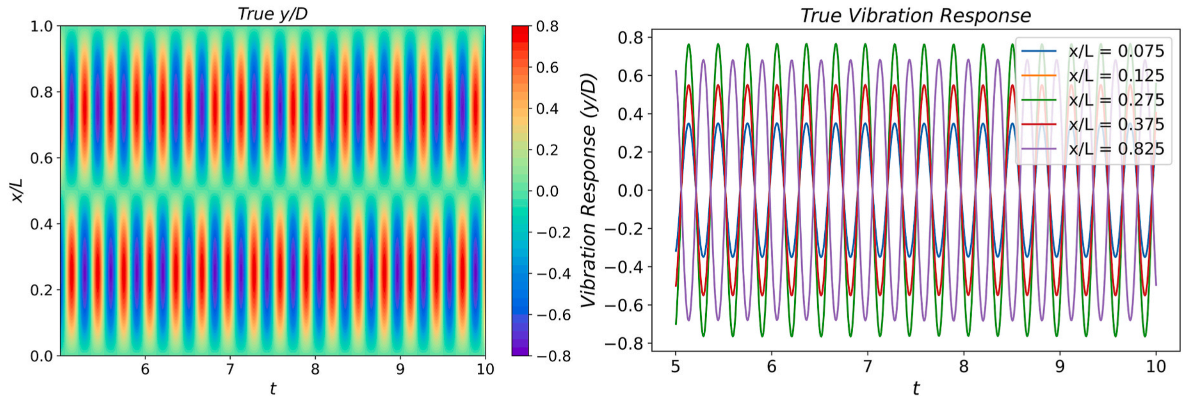

Fig. 9. The numerical solution of the top-tensioned riser. (a) Displacement field; (b) The displacement-time history at different positions.

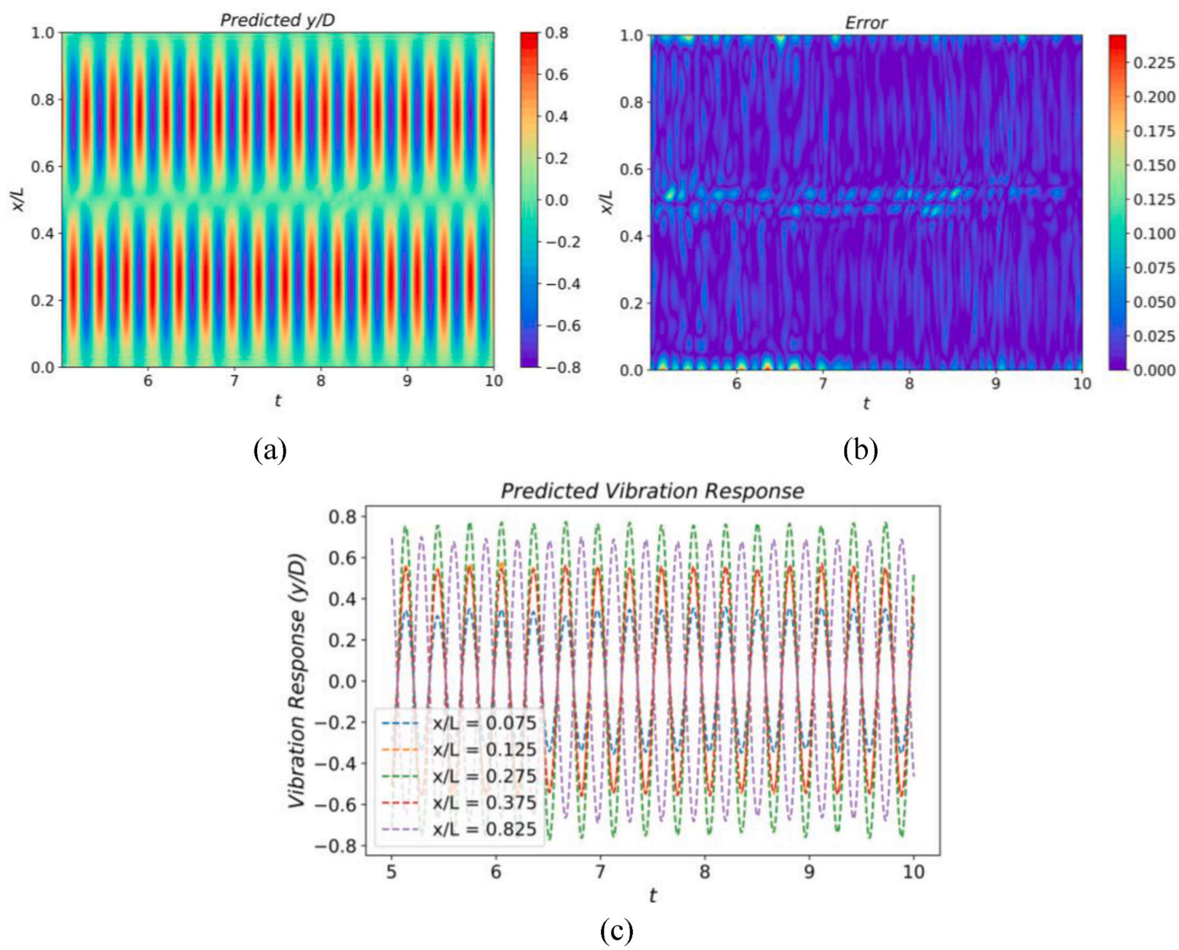

Fig. 10. Reconstruction results of the riser's displacement field based on the traditional DL model. (a) Displacement field; (b) Reconstruction error; (c) Displacement-time history at different positions.

of the hinged flexible cylindrical structure can be calculated by $f = \frac{i^2\pi}{2}\sqrt{\frac{EI}{m_s L^4}}$. Fig. 4(b)–(k) illustrates the first 10 mode shapes of the flexible cylinder.

3.2. Training of model

The deep modal model proposed in Section 2 and traditional DL model are then utilized to reconstruct the entire displacement time history on the riser. In the pre-training of the deep modal model, the features of the first 10 mode shapes of the top tension riser are extracted. The fully connected neural network (FCNN) is used to represent the mode shapes, with the input being the coordinate x and the output being the normalized mode shapes of the first 10 modes. The training dataset consists of the first 10 mode shapes described in Section 3.1.2 (as shown in Fig. 5(a)). To simulate the scenario of limited sensor placement in actual engineering, response time history data from 19 nodes (5–10 s) selected from the 201 numerical discrete solutions is used as the training dataset (as shown in Fig. 5(b)). The computing platform and environment configuration utilized for all model training in this study are summarized in Table 4. The hyperparameters specific to the models

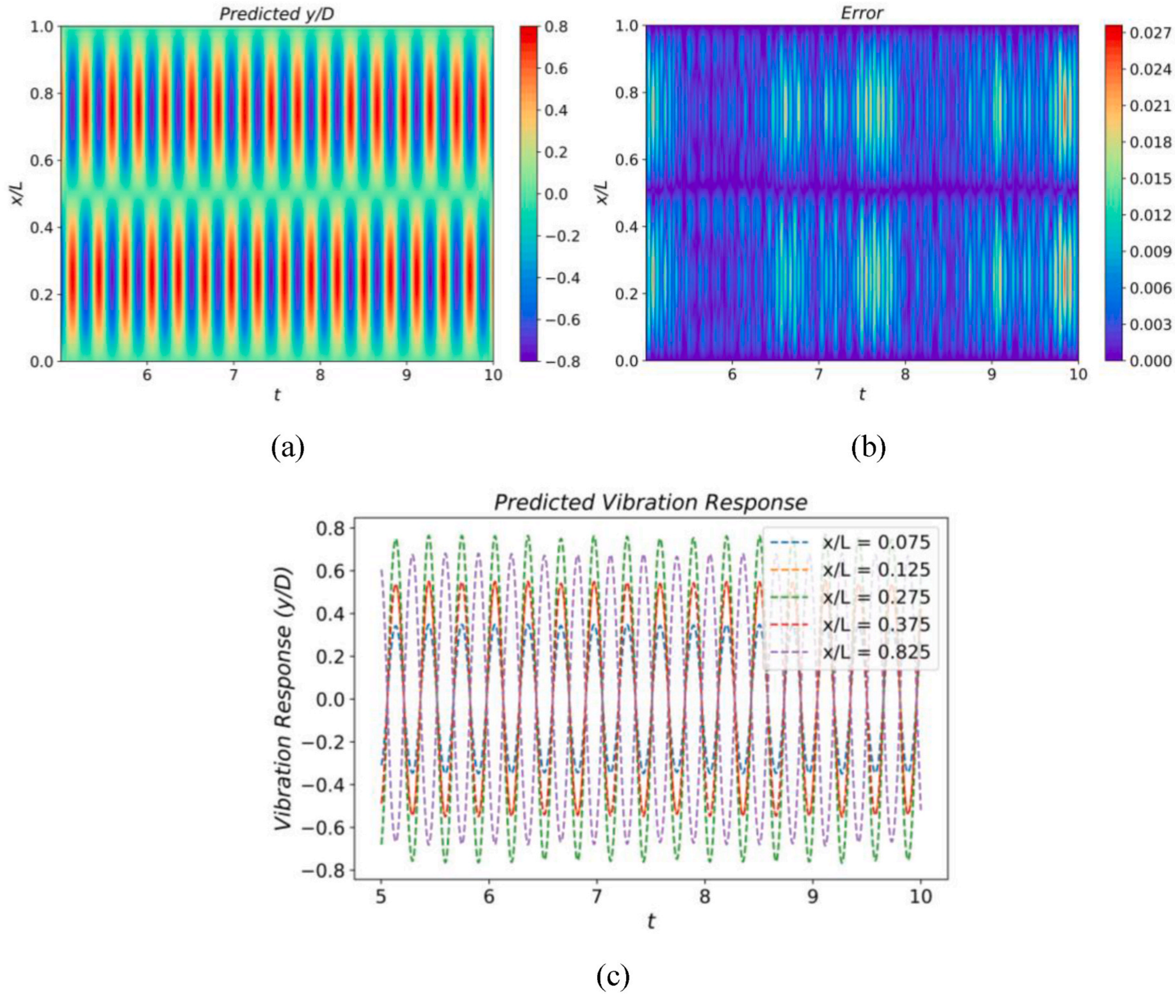

Fig. 11. Reconstruction results of the riser displacement field based on the deep modal model. (a) Displacement field; (b) Reconstruction error (c) Time history of displacement at different positions.

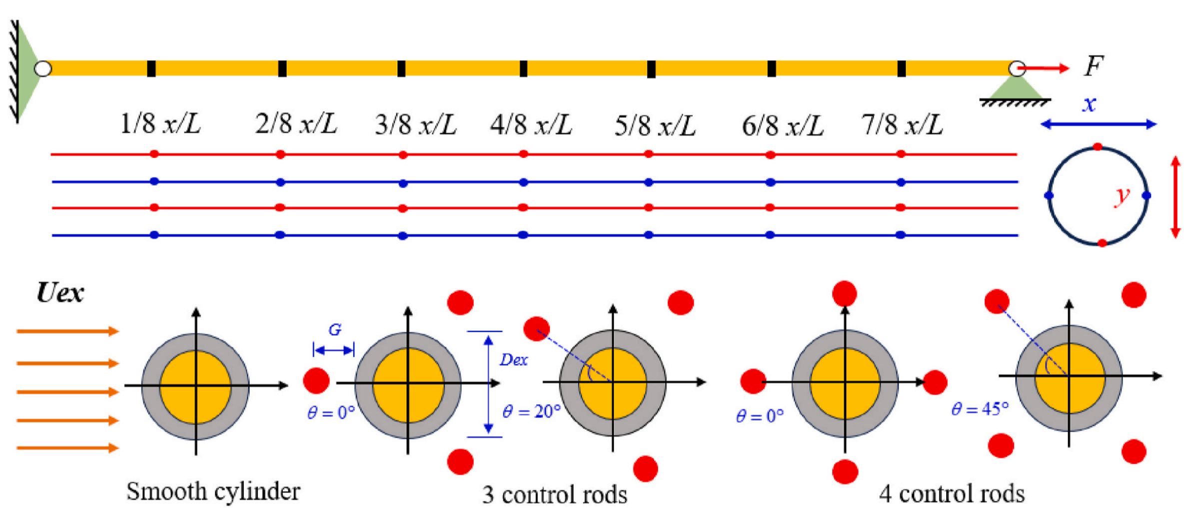

Fig. 12. The arrangement of strain gauge and different working conditions in the experiment.

training are presented in Table 5. The loss functions of the pre-training process and the main network training process are illustrated in Figs. 6 and 7. In particular, at the end of main network model training, the learning rate of the model is adjusted to ensure that the loss function value of the two models is less than 1E-4.

3.3. Reconstruction result

Fig. 8 shows the prediction results of the first 10 normalized mode shapes obtained by the FCNN. It can be seen that the predictions are highly consistent with the mode shapes obtained using the FDM method.

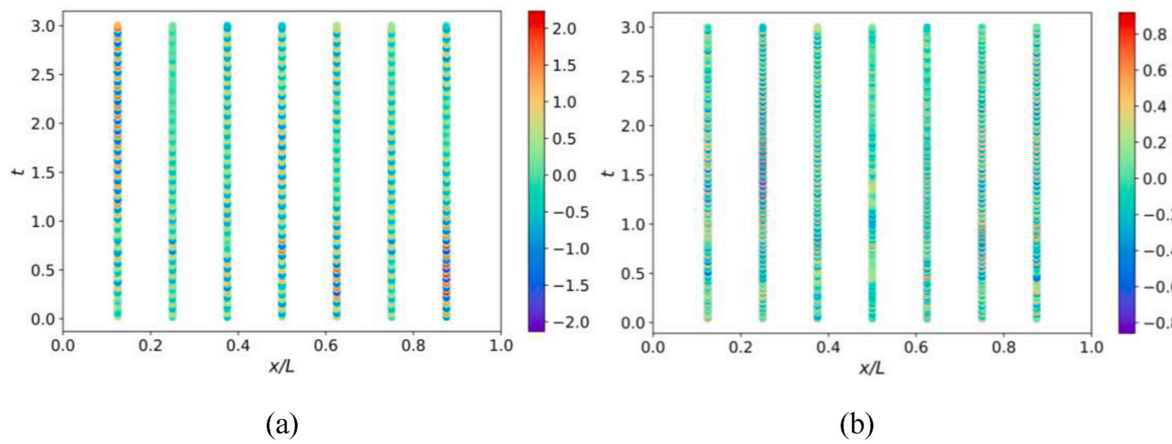

Fig. 13. Training dataset for the smooth flexible cylinder ($U = 1.00$ m/s). (a) CF direction; (b) IL direction.

Table 6
The hyperparameters specific to the model training.

Case	Type	Model architecture	Activation function	Optimizer	Learning rate	Initializer
CF, Smooth	FCNN	4*256	Sin	Adamax	1E-4	Glorot uniform
	LSTM	128 + 4*256 + 128	Tanh/Sigmoid		1E-3 (30000) +5E-4 (40000) +1E-4 (10000)	
IL, Smooth	FCNN	4*256	Sin	Adamax	1E-4	Glorot uniform
	LSTM	128 + 4*256 + 128	Tanh/Sigmoid		1E-3 (30000) +5E-4 (40000) +1E-4 (10000)	

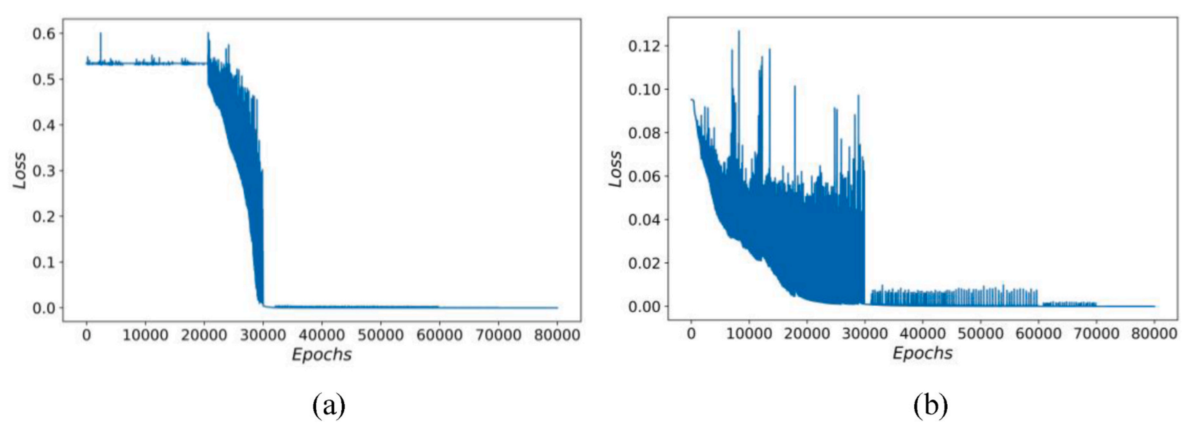

Fig. 14. Loss function for the smooth flexible cylinder ($U = 1.00$ m/s). (a) CF direction; (b) IL direction.

In order to compare the accuracy of the traditional DL model and deep modal model, Fig. 9(a) shows the numerical solutions at 201 locations along the top-tensioned riser, solved using FDM and the 4-RK method. Fig. 9(b) presents the displacement time history curves at five randomly selected locations ($x/L = 0.075, 0.125, 0.275, 0.375, 0.825$) outside of the training set. Figs. 10 and 11 respectively display the reconstructed displacement results of the riser based on 19 sparse sensor displacement-time history data, using the traditional DL model and the deep modal model, along with the absolute error values. The formula for calculating the absolute error is as follows:

$$Error = \left|\widehat{y}_{pre} - y_{true}\right| \tag{13}$$

where $\widehat{y}_{pre}$ represents the model's predicted value, and y_{true} denotes the numerical result.

Comparing the results of Figs. 9 and 10, it can be observed that the traditional DL model essentially fits the discrete data space, and its fitting accuracy largely depends on the spatial distribution density of the labeled data. Therefore, although the traditional DL model captures the overall characteristics of the riser's displacement field, the error in regions with significant local variation is larger due to the sparsity of the labeled data. In this case, the displacement-time history data from 19 discrete locations are evenly distributed along the riser, but there is no labeled data at either end. As shown in Fig. 10(b), the error is relatively large at the locations near the two ends of the riser and in the middle, where there is no labeled data constraint. Notably, the error at the middle of the riser ($x/L = 0.5$) is relatively large. This is because the riser's vibration is primarily dominated by the second mode, with a wave node near the middle, making the vibration pattern more complex.

Due to the correlation between the vibration responses at different spatial locations of the riser, it is difficult for traditional DL models to capture this feature when the spatial locations are sparsely distributed.

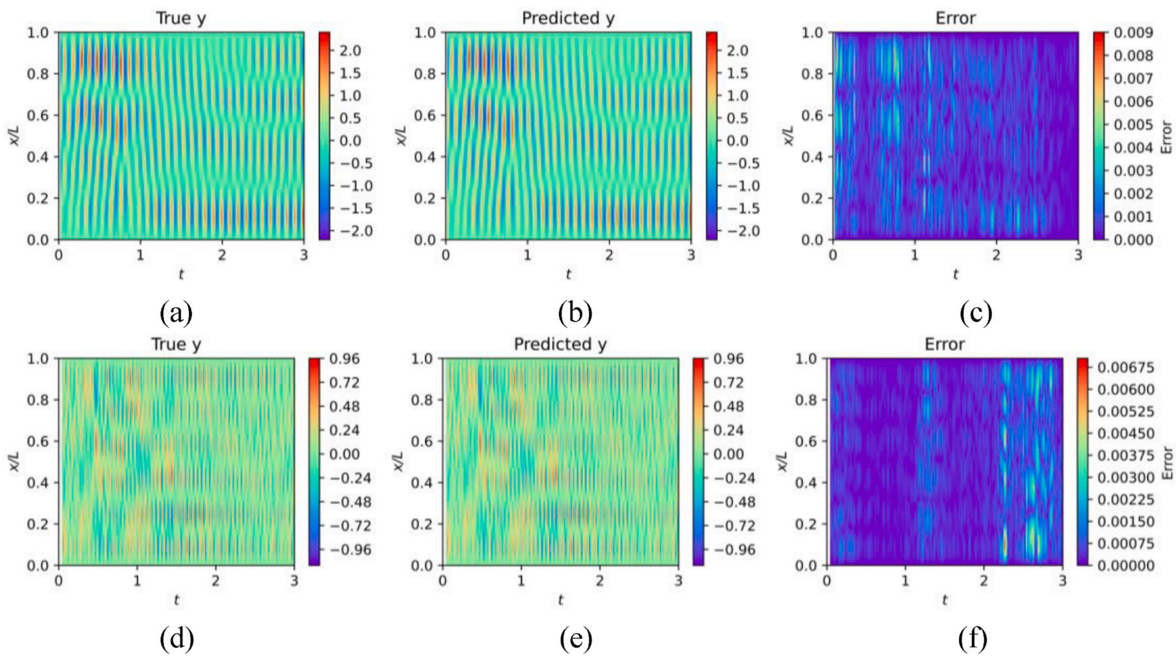

Fig. 15. Reconstructed displacement results for the smooth flexible cylinder ($U = 1.00$ m/s). (a–c) CF direction; (d–f) IL direction.

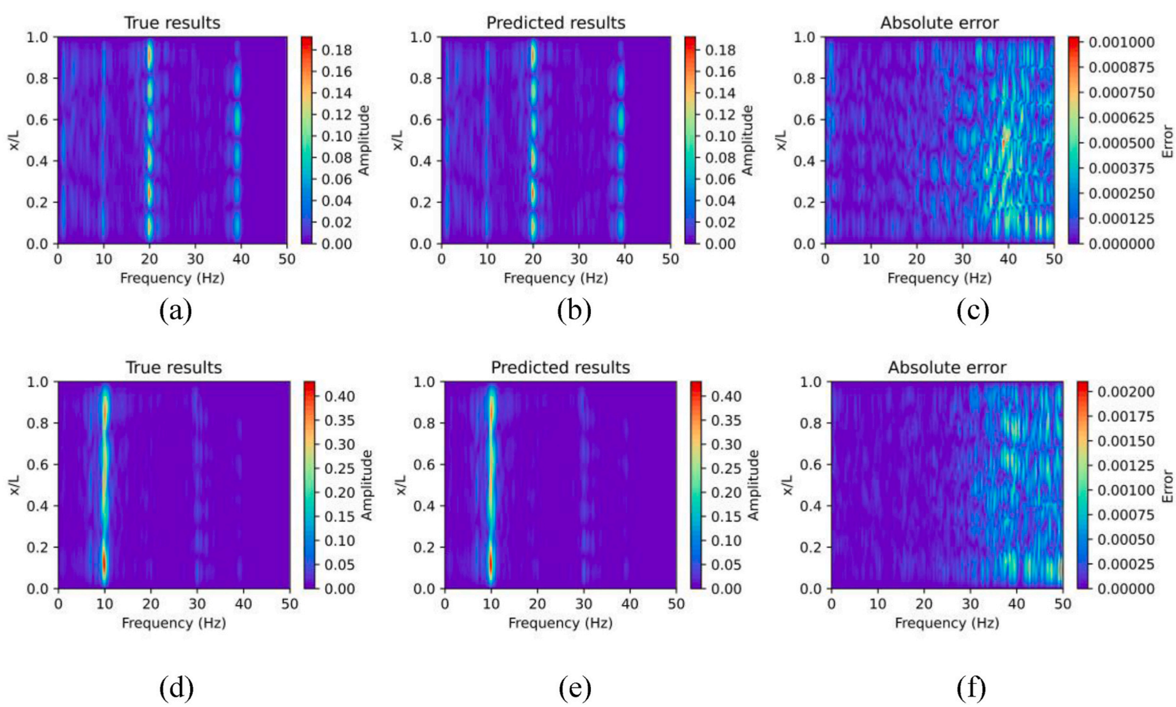

Fig. 16. Frequency spectrum of reconstructed displacement response for the smooth flexible cylinder ($U = 1.00$ m/s). (a–c) CF direction; (d–f) IL direction.

However, for the deep modal model, the embedding of the riser's modes establishes spatial physical constraints between different spatial points, making the model's predictions more consistent with the actual results (see Fig. 11). The output of the model consists of the ten modal weights of the riser. As the model is trained, the deep modal model successfully captures the characteristics of the second mode. As shown in Fig. 11(a) and (b), the predictions of the deep modal model are highly consistent with the numerical solutions. The maximum error value is less than 0.027.

4. Reconstruction of experimental data based on deep modal model

In this section, the deep modal method is applied to reconstruct experimental data (sparse sensor data). These experimental conditions include a smooth flexible cylinder, the flexible cylinders with 3 or 4 control rods. The detailed experimental procedures can be found in Lu et al. (2019, 2020). In this study, the selected experimental conditions had a flow velocity of 1 m/s (the maximum flow velocity during the experiment, characterized by complex flow patterns). During the experiment, strain responses in the in-line (IL) and cross-flow (CF)

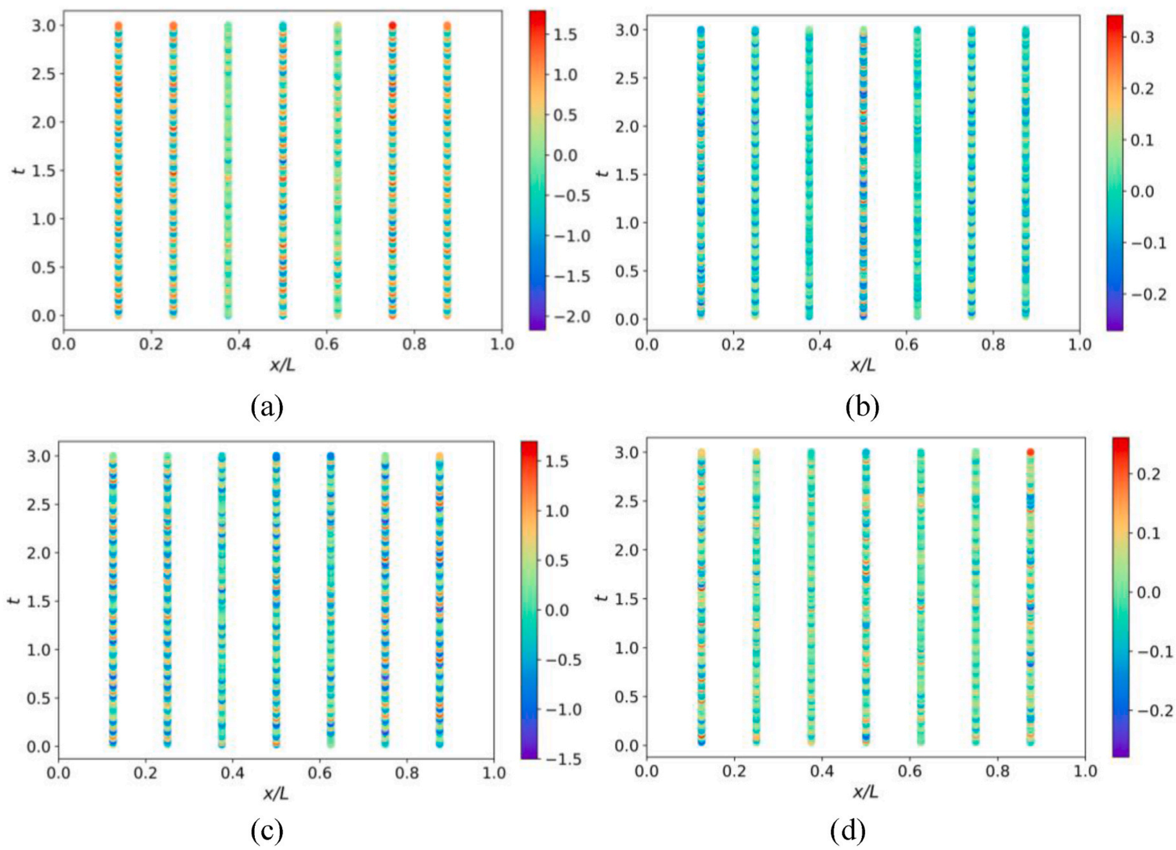

Fig. 17. Training dataset for the flexible cylinder with 3 control rods ($U = 1.00$ m/s). (a) CF direction, Attack angle 0°; (b) IL direction, Attack angle 0°; (c) CF direction, Attack angle 20°; (d) IL direction, Attack angle 20°.

Table 7
The hyperparameters specific to the model training.

Case	Type	Model architecture	Activation function	Optimizer	Learning rate	Initializer
CF, 0°	FCNN LSTM	4*256 128 + 4*256 + 128	Sin Tanh/Sigmoid	Adamax	1E-4 5E-3 (30000) +5E-4 (40000) +1E-4 (10000)	Glorot uniform
IL, 0°	FCNN LSTM	4*256 128 + 4*256 + 128	Sin Tanh/Sigmoid	Adamax	1E-4 5E-3 (30000) +5E-4 (40000) +1E-4 (10000)	Glorot uniform
CF, 20°	FCNN LSTM	4*256 128 + 4*256 + 128	Sin Tanh/Sigmoid	Adamax	1E-4 5E-3 (30000) +5E-4 (40000) +1E-4 (10000)	Glorot uniform
IL, 20°	FCNN LSTM	256 128 + 4*256 + 128	Sin Tanh/Sigmoid	Adamax	1E-4 5E-3 (30000) +5E-4 (40000) +1E-4 (10000)	Glorot uniform

directions are measured by 7 sets of strain gauges attached to the cylinder model. The distribution of the strain gauges is shown in Fig. 12. By utilizing the relationship between strain and displacement, the displacements in the IL and CF directions at the measurement points on the cylinder model are obtained. Due to the availability of discrete data from only 7 positions, the DL model is used during pre-training to extract features of the first 7 modes of the flexible cylindrical structure. To verify the model's effectiveness, displacement reconstruction for 161 position points on the flexible cylinder is performed based on traditional modal analysis methods (Lie and Kaasen, 2006; Trim et al., 2005), and the results are compared with the predictions from the deep modal model. In this section, the mode shape training dataset is generated using analytical methods. For a flexible cylindrical structure with hinged supports at both ends, its i-th mode shape can be expressed as (Lie and Kaasen, 2006; Trim et al., 2005):

$$\phi_i(x) = \sin(i\pi x / L) \tag{14}$$

The process of extracting mode shape features using the FCNN model is consistent with that described in Section 3.2. The training loss function and mode shape prediction results are provided in Appendix A. Since the experimental data used in this section all pertain to the same flexible cylindrical model, the same pre-trained FCNN mode representation model is used for transfer learning in subsequent sections.

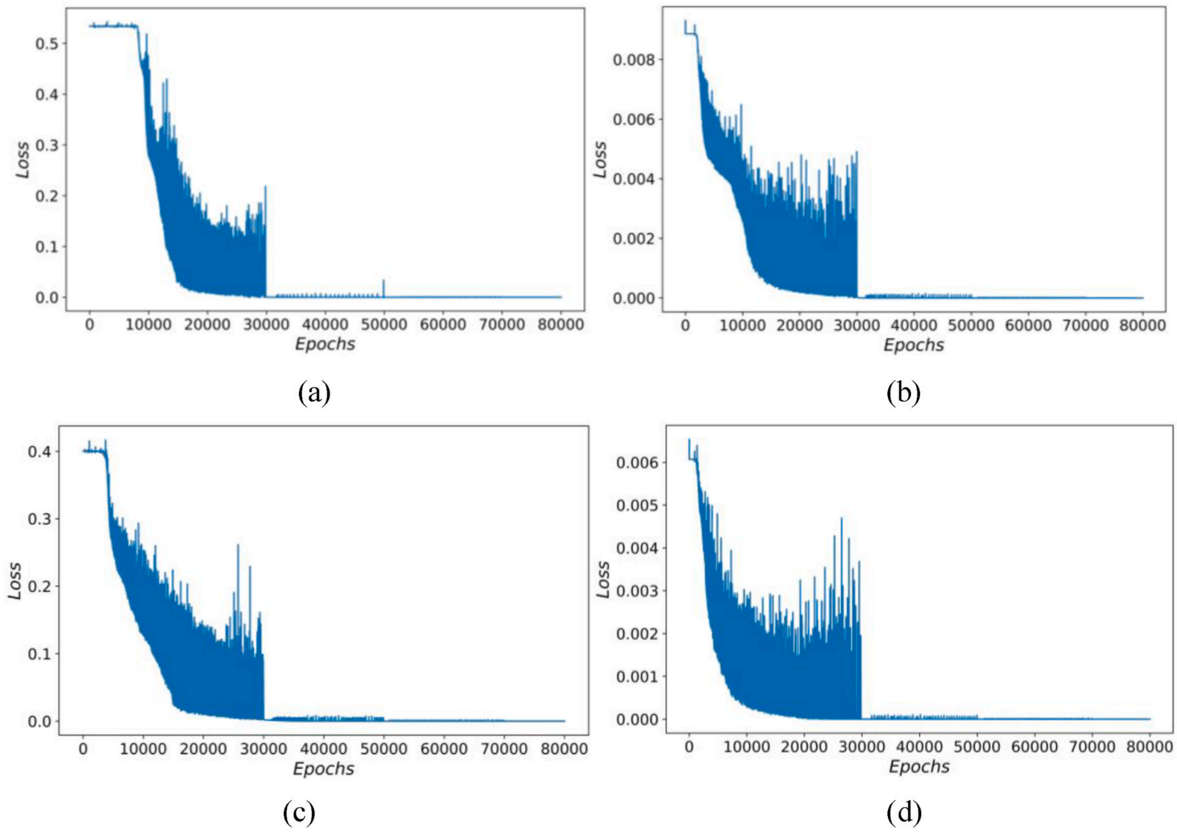

Fig. 18. Loss function for the flexible cylinder with 3 control rods ($U = 1.00$ m/s). (a) CF direction, Attack angle 0°; (b) IL direction, Attack angle 0°; (c) CF direction, Attack angle 20°; (d) IL direction, Attack angle 20°.

4.1. The smooth flexible cylinder

Fig. 13 shows the displacement responses in the CF and IL directions at 7 positions on the smooth flexible cylinder model under a uniform flow velocity of $U = 1$ m/s, with a randomly selected time duration of 3 s. Due to the complexity of the vibration modes during the experiment, the corresponding modal weight functions are also more intricate. Therefore, the more complex LSTM model is employed. During the training process, different learning rates are used to train the model (as shown in Table 6), and the variation of the model's loss function is shown in Fig. 14, with the loss function values all decreasing below 1E-4. The training platform and environment for all models are shown in Table 4.

Figs. 15 and 16 present the reconstructed displacement response and corresponding frequency spectrum for a smooth flexible cylinder subjected to a uniform flow velocity of $U = 1.00$ m/s. The results illustrate the comparison between the true displacement data, the predicted data from the deep modal model, and the associated error for both the CF and IL directions. From Fig. 15(a) and (d), it is evident that the displacement along the length of the flexible cylinder in both the CF and IL directions varies significantly, with distinct regions of high and low displacement, indicating that higher-order modes significantly influence the vibration. On the other hand, the prediction results of the deep mode model are highly consistent with those of the modal analysis method, both in terms of displacement response and the corresponding frequency spectrum (as shown in Figs. 15 and 16). In the CF direction, as the dominant vibrational mode transitions from the third to the fourth order, significant changes in the modal weight functions occur, leading to increased prediction errors. Nonetheless, the deep modal model effectively captures the modal competition behavior during the vibration process of the flexible cylinder. These results demonstrate that the proposed deep modal model can effectively reconstruct the displacement field of the smooth flexible cylinder during experiments.

4.2. The flexible cylinder with 3 or 4 control rods

Furthermore, to validate the generalization of the proposed deep modal model, it is applied to more complex working conditions. Fig. 17 shows the displacement responses in both the CF and IL directions at 7 positions on the flexible cylinder model with 3 control rods (the attack angles are 0° and 20° respectively, as shown in Fig. 12), under a uniform flow velocity of $U = 1$ m/s, over a randomly selected time duration of 3 s. The hyperparameter settings for model training are shown in Table 7. Models are also trained using different learning rates. The loss function descent process for the four models is illustrated in Fig. 18. The loss function value of all models reaches below 1E-4 within the preset training epochs.

Figs. 19 and 20 illustrate the VIV response and corresponding frequency spectrum of the flexible cylinder with 3 control rods arranged at angles of attack of 0° and 20° (including results obtained from modal analysis method and the deep modal model). From Figs. 19 and 20, it can be observed that the deep modal model consistently demonstrates excellent predictive capabilities. The vibration response of the entire flexible cylinder, as reconstructed by the model, shows a regular variation over time. The reconstruction results (the displacement response and corresponding frequency spectrum are included) of the deep modal model are highly consistent with those of the modal analysis method.

Fig. 21 presents the displacement responses in both the CF and IL directions at 7 different positions on the flexible cylinder model, equipped with 4 control rods, with attack angles of 0° and 45° (as shown in Fig. 12), respectively, under a uniform flow velocity of $U = 1$ m/s, over a randomly selected time interval of 3 s. The hyperparameter settings used for model training are outlined in Table 8. Models are trained with various learning rates, and the loss function descent process for all

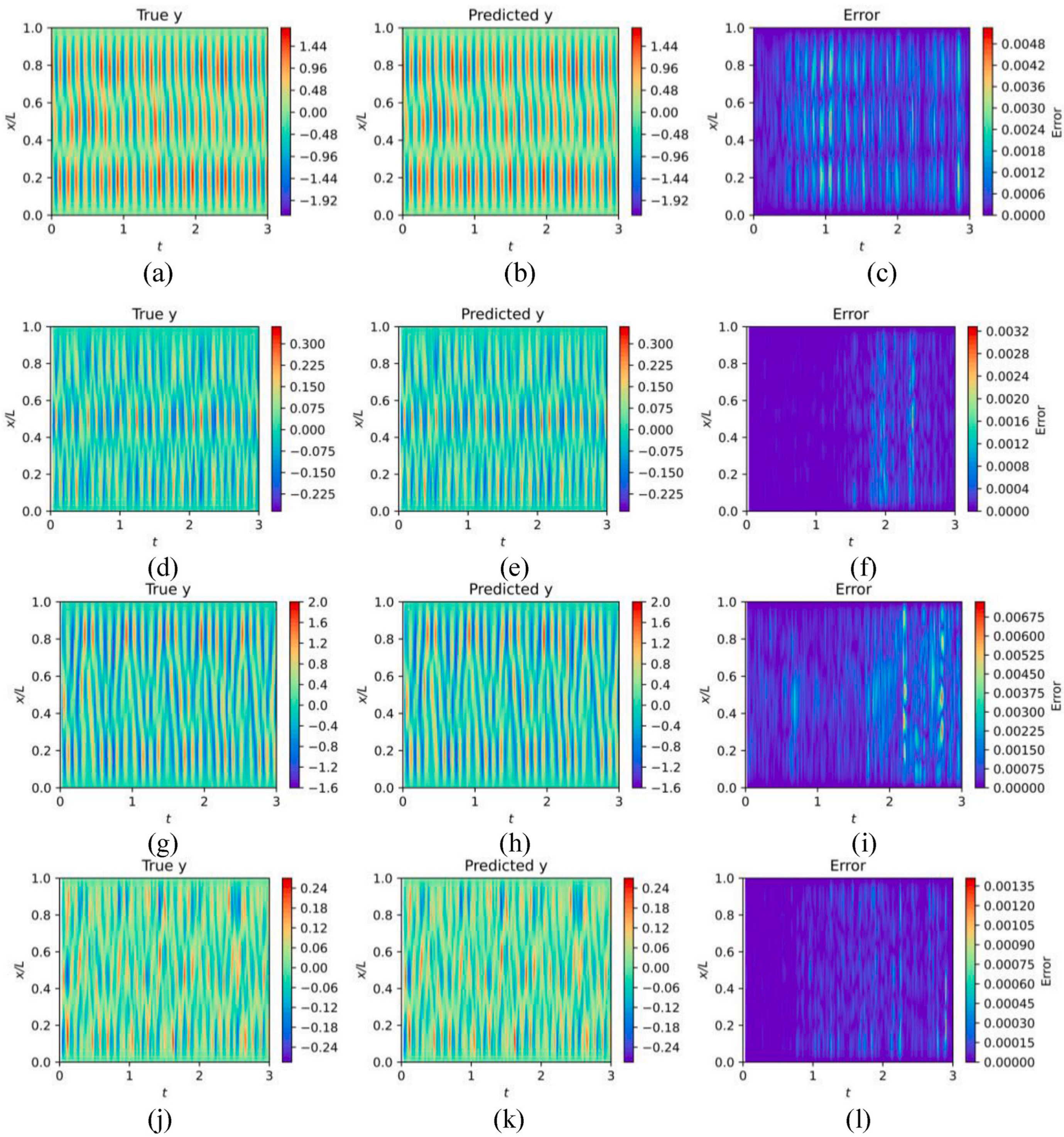

Fig. 19. Reconstructed displacement results for the flexible cylinder with 3 control rods ($U = 1.00$ m/s). (a–c) CF direction, Attack angle 0°; (d–f) IL direction, Attack angle 0°; (g–i) CF direction, Attack angle 20°; (j–l) IL direction, Attack angle 20°.

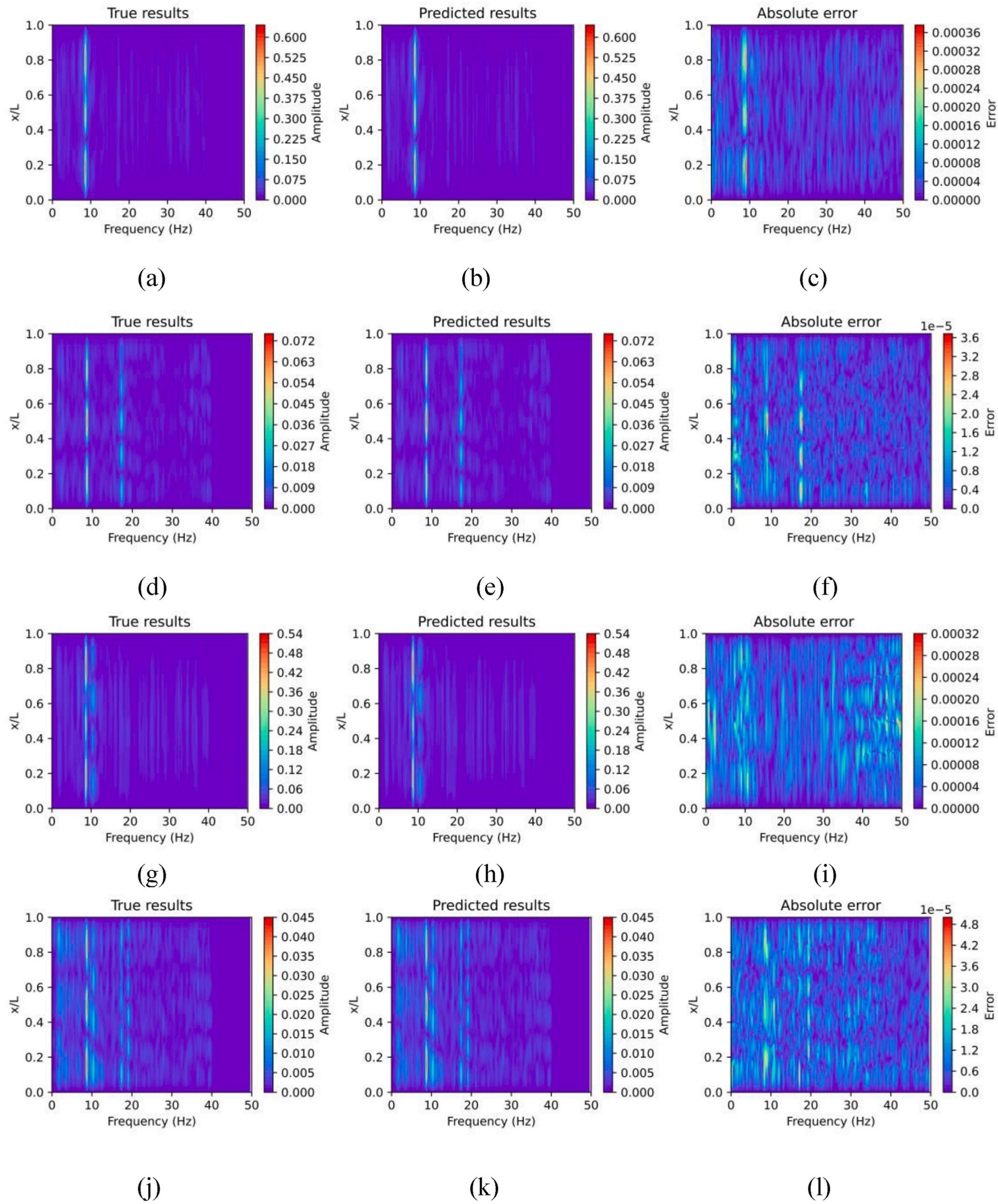

Fig. 20. Frequency spectrum of reconstructed displacement response for the flexible cylinder with 3 control rods ($U = 1.00$ m/s). (a–c) CF direction, Attack angle 0°; (d–f) IL direction, Attack angle 0°; (g–i) CF direction, Attack angle 20°; (j–l) IL direction, Attack angle 20°.

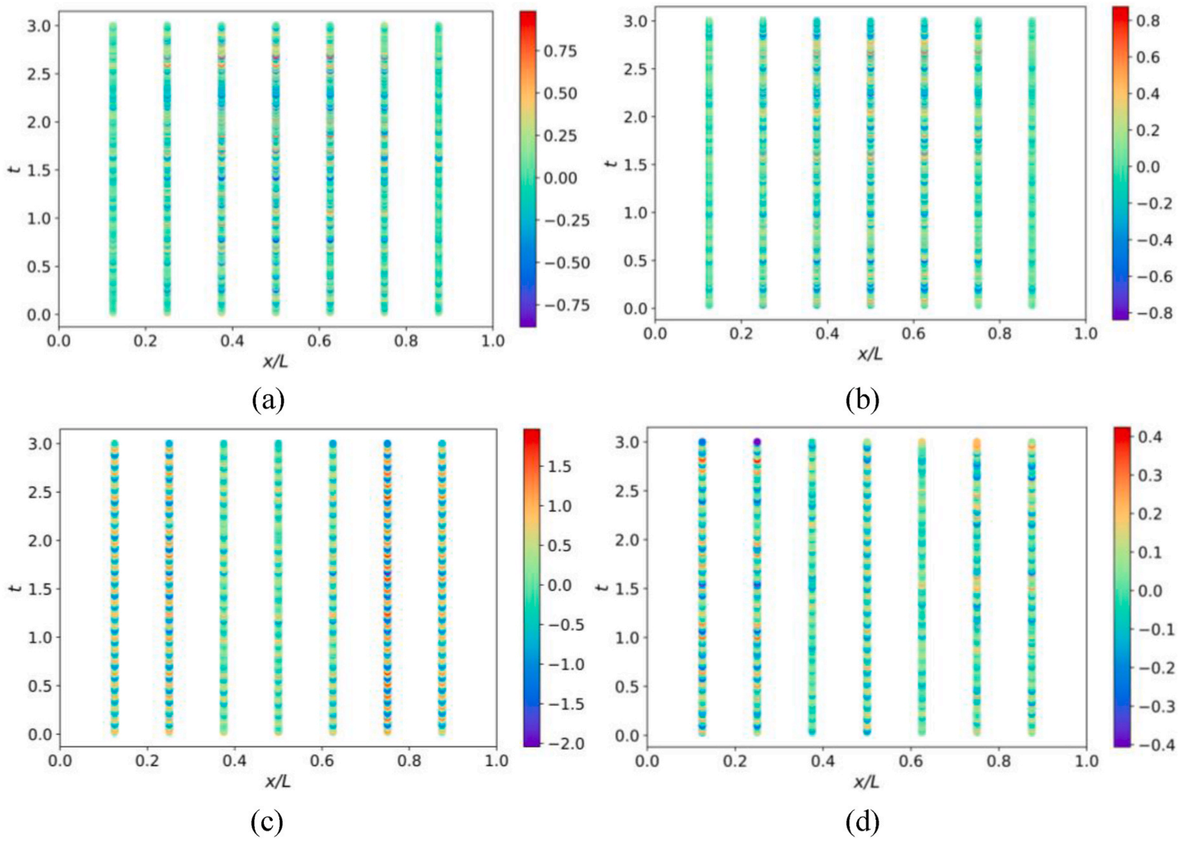

Fig. 21. Training dataset for the flexible cylinder with 4 control rods (U = 1.00 m/s). (a) CF direction, Attack angle 0°; (b) IL direction, Attack angle 0°; (c) CF direction, Attack angle 45°; (d) IL direction, Attack angle 45°.

Table 8
The hyperparameters specific to the model training.

Case	Type	Model architecture	Activation function	Optimizer	Learning rate	Initializer
CF, 0°	FCNN LSTM	4*256 128 + 4*256 + 128	Sin Tanh/Sigmoid	Adamax	1E-4 5E-3 (30000) +5E-4 (40000) +1E-4 (10000)	Glorot uniform
IL, 0°	FCNN LSTM	4*256 128 + 4*256 + 128	Sin Tanh/Sigmoid	Adamax	1E-4 5E-3 (30000) +5E-4 (40000) +1E-4 (10000)	Glorot uniform
CF, 45°	FCNN LSTM	4*256 128 + 4*256 + 128	Sin Tanh/Sigmoid	Adamax	1E-4 5E-3 (30000) +5E-4 (40000) +1E-4 (10000)	Glorot uniform
IL, 45°	FCNN LSTM	256 128 + 4*256 + 128	Sin Tanh/Sigmoid	Adamax	1E-4 5E-3 (30000) +5E-4 (40000) +1E-4 (10000)	Glorot uniform

four models is depicted in Fig. 22. Notably, the loss function values for all models fell below 1E-4 within the predefined number of training epochs.

Figs. 23 and 24 shows the VIV response and corresponding frequency spectrum of the flexible cylinder with 4 control rods arranged at attack angles of 0° and 45°, comparing results from the modal analysis method and the deep modal model. As with the 3-control rod configuration, the deep modal model's predictions align closely with those from the modal analysis method. This demonstrates the deep modal model's ability to accurately capture the dynamic behavior of the flexible cylinder and effectively reconstruct vibration patterns influenced by various control rod configurations and attack angles.

Based on the above analysis, it can be concluded that the proposed deep modal model is not only applicable to riser displacement reconstruction in various scenarios but also demonstrates high precision and generalization capability. This highlights the model's robustness and accuracy in simulating complex vortex-induced vibrations.

5. Conclusions

In this paper, the deep modal model combines modal analysis with a long short-term memory (LSTM) network to achieve high-precision reconstruction of the global VIV response of flexible cylindrical structures using data from sparsely placed sensors. The applicability of deep modal model to flexible cylinder is verified based on a numerical case study. Subsequently, the responses of a smooth cylinder, as well as

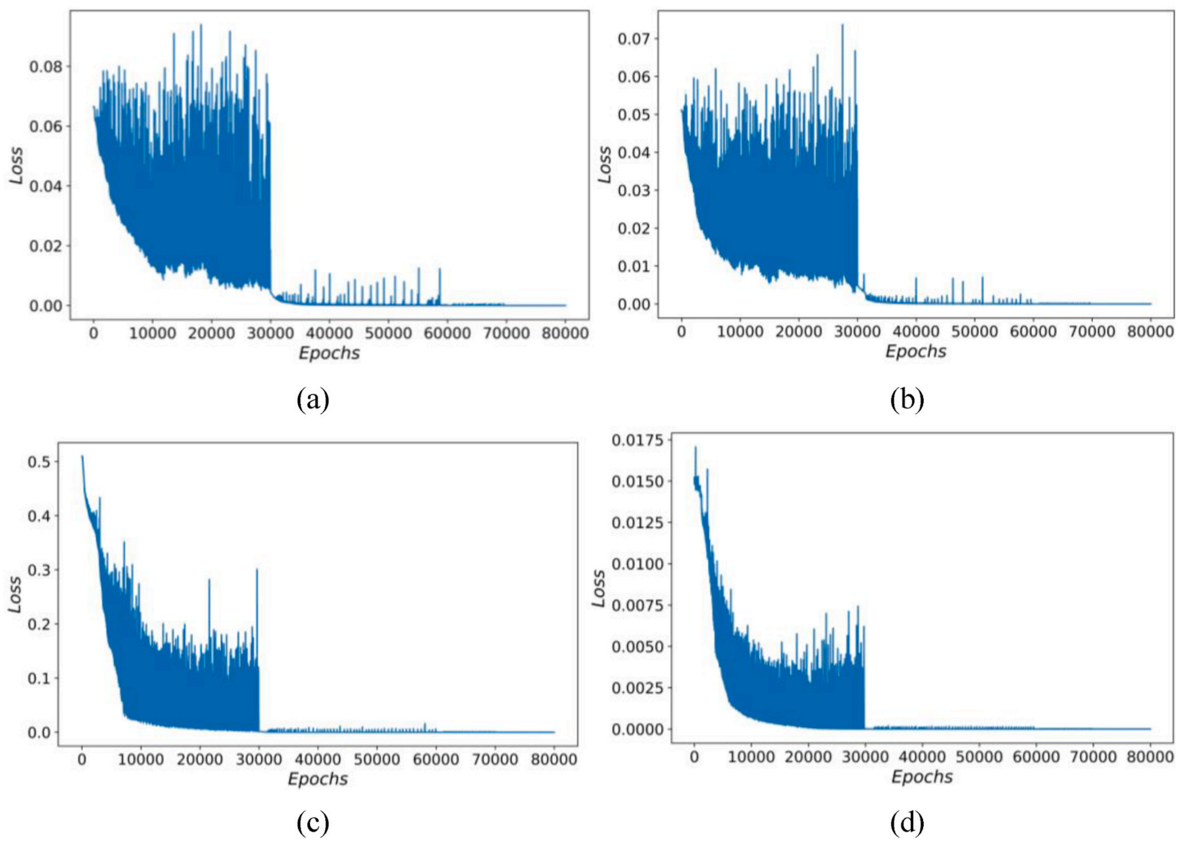

Fig. 22. Loss function for the flexible cylinder with 4 control rods ($U = 1.00$ m/s). (a) CF direction, Attack angle 0°; (b) IL direction, Attack angle 0°; (c) CF direction, Attack angle 45°; (d) IL direction, Attack angle 45°.

cylinders with 3 or 4 control rods, are reconstructed using sparse sensor data from 7 locations in the experiment. The main conclusions are obtained as follows.

(1) A deep modal model is introduced for the reconstruction of VIV responses in flexible cylindrical structures using sparse sensor data. This method utilizes DL models to represent the modal shapes and modal weight functions of the displacement of a flexible cylinder. The pre-trained modal model enabled the transfer of implicit physical laws into the LSTM network, further enhancing the accuracy and robustness of the reconstruction process. Finally, sparse labeled data is used to extract the time-varying characteristics of modal weights at different orders. Under the physical constraints of the structural modes, the global displacement field of the flexible cylinder is reconstructed.
(2) The effectiveness of the proposed deep modal model is demonstrated through a numerical case study involving a top-tensioned riser. The vortex-induced vibration dynamics of the top-tensioned riser are modeled based on an acceleration-coupled van der Pol wake oscillator model and solved using the finite difference method and the 4-RK method. The displacement-time history of the entire riser is reconstructed based on the displacement-time history at 19 selected node positions. The results indicate that the constructed deep modal model performs well in the numerical case, with its reconstructed displacement field showing greater reliability compared to results from traditional DL models.
(3) The deep modal model is applied to experimental cases, where the global displacement field of a smooth flexible cylinder, as well as flexible cylinders with 3 and 4 control rods, is reconstructed based on 7 sparsely arranged sensor data. By transferring the pre-trained modal features into the LSTM model, the reconstruction of displacement is performed under the dual constraints of modal physics and sparse data. The results show that the displacement reconstruction (included the displacement response and corresponding frequency spectrum) of the proposed deep modal model is highly consistent with traditional modal analysis methods. The deep modal model accurately captures the dynamic behavior of the flexible cylinders and effectively reconstructs the vibration modes influenced by various control rod configurations and attack angles. Its robustness and accuracy in simulating complex vortex-induced vibration problems make it a powerful tool for monitoring large-scale civil and ocean structures.

The proposed deep modal model can be combined with more advanced deep learning models (such as transformer models or graph neural networks) to improve its predictive capability in handling more complex vibration modes and nonlinear behaviors. Additionally, the integration of multimodal data (such as strain, acceleration, and pressure) into the model can enhance its prediction accuracy and robustness in complex vibration problems, allowing for better capture of various dynamic behaviors in structures. One limitation of this study is that the model's generalizability remains restricted, as it has primarily been validated on flexible cylindrical structures with vortex-induced vibrations. Further testing is needed on more complex fluid-structure interaction problems or different structural types. Moreover, the introduction of the LSTM network increases computational complexity, which may present challenges for real-time applications in large-scale structures.

CRediT authorship contribution statement

Yangyang Liao: Writing – review & editing, Writing – original draft, Visualization, Methodology, Investigation, Formal analysis, Conceptualization. **Hesheng Tang:** Writing – review & editing, Supervision, Project administration, Methodology, Funding acquisition, Data

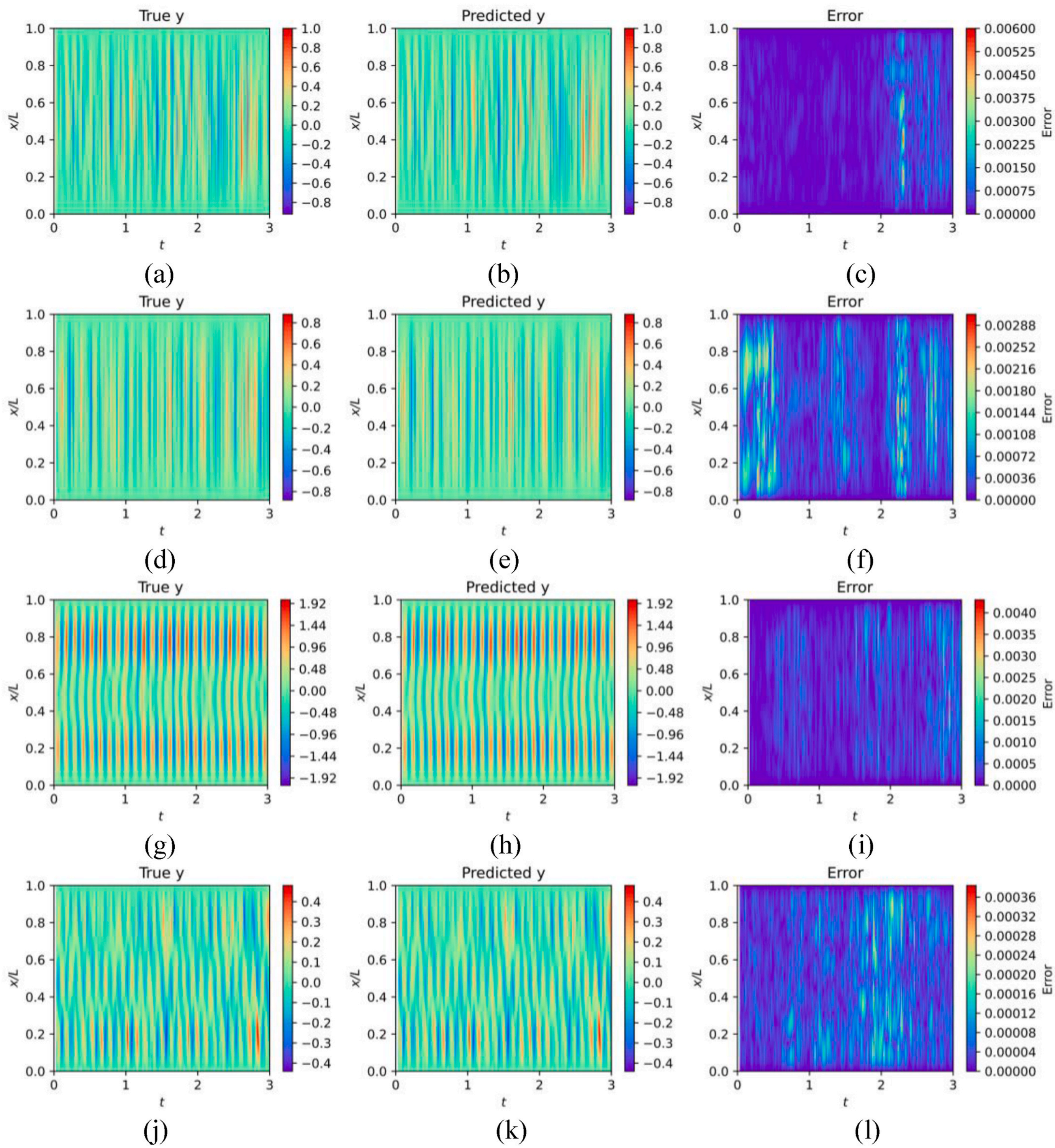

Fig. 23. Reconstructed displacement results for the flexible cylinder with 4 control rods ($U = 1.00$ m/s). (a–c) CF direction, Attack angle 0°; (d–f) IL direction, Attack angle 0°; (g–i) CF direction, Attack angle 45°; (j–l) IL direction, Attack angle 45°.

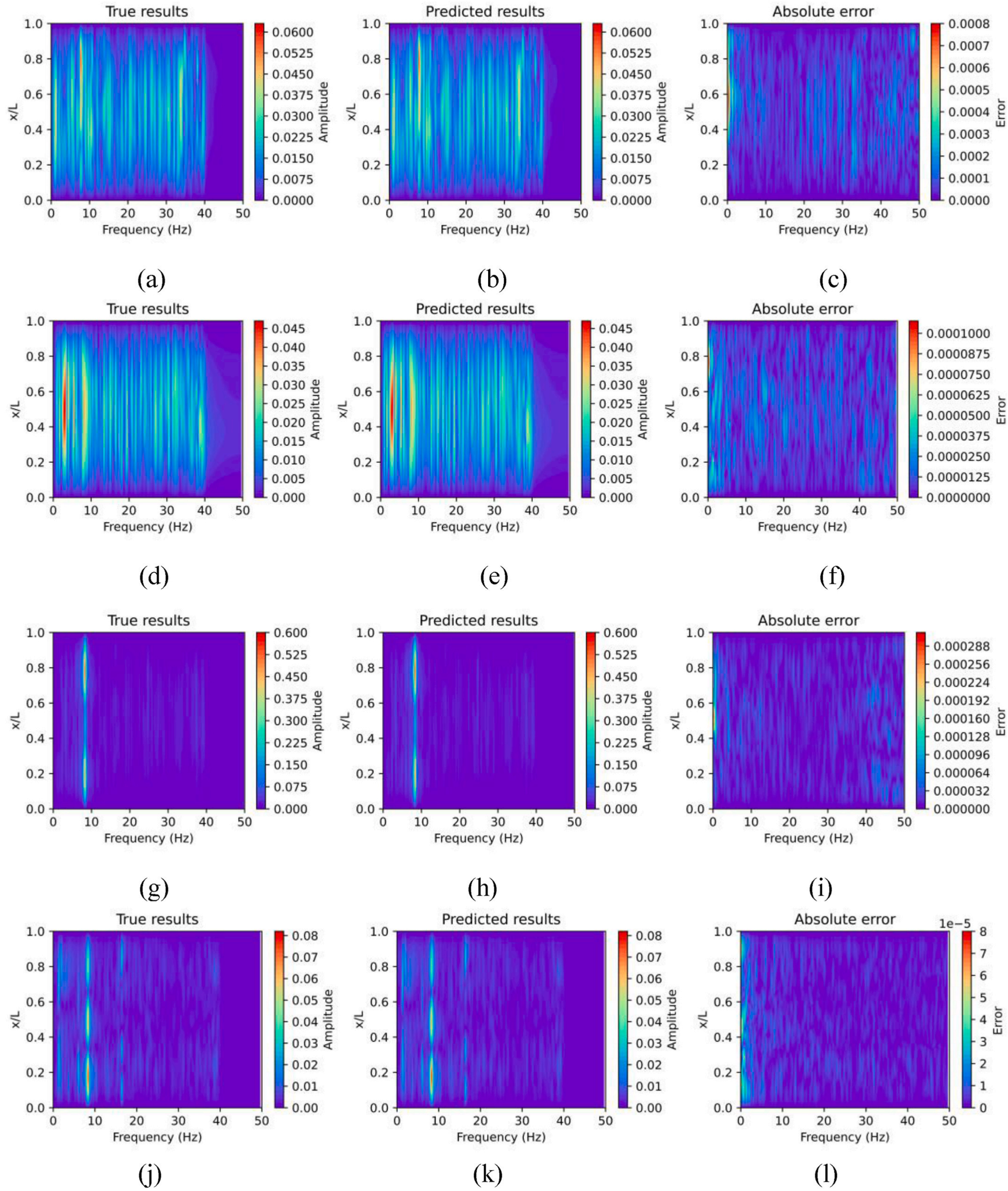

Fig. 24. Frequency spectrum of reconstructed displacement response for the flexible cylinder with 4 control rods ($U = 1.00$ m/s). (a–c) CF direction, Attack angle 0°; (d–f) IL direction, Attack angle 0°; (g–i) CF direction, Attack angle 45°; (j–l) IL direction, Attack angle 45°.

curation, Conceptualization. **Liyu Xie:** Writing – review & editing, Validation, Supervision.

Declaration of competing interest

The authors declare that they have no known competing financial interests or personal relationships that could have appeared to influence the work reported in this paper.

Acknowledgments

This research was supported by National Natural Science Foundation of China (52378184).

Appendix A

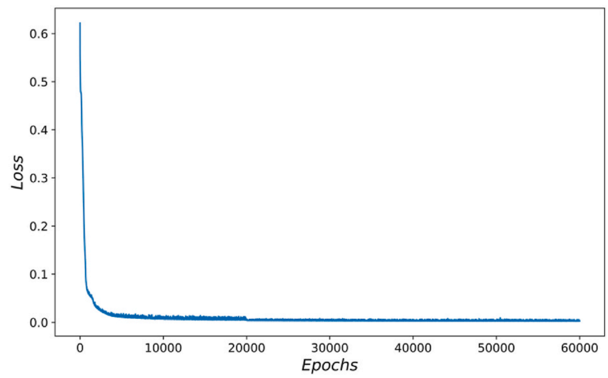

A. 1. Loss functions during pre-training process.

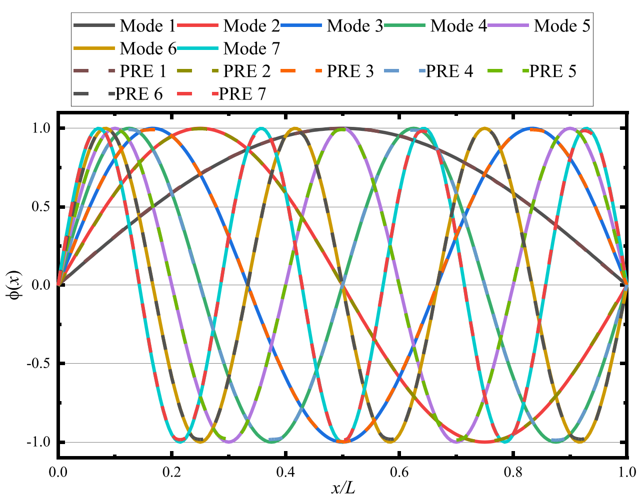

A. 2. Prediction results of normalized mode shapes by FCNN.

References

Amato, F., Guignard, F., Robert, S., Kanevski, M., 2020. A novel framework for spatio-temporal prediction of environmental data using deep learning. Sci. Rep. 10 (1), 22243.

Blevins, R.D., 1977. Flow-induced Vibration. New York.

Brener, B.P., Cruz, M.A., Macedo, M.S., Thompson, R.L., 2024. A highly accurate strategy for data-driven turbulence modeling. Comput. Appl. Math. 43 (1), 59.

Chaplin, J.R., Bearman, P.W., Cheng, Y., Fontaine, E., Graham, J.M.R., Herfjord, K., et al., 2005. Blind predictions of laboratory measurements of vortex-induced vibrations of a tension riser. J. Fluid Struct. 21 (1), 25–40.

Du, Z.F., Zhu, H.M., Yu, J.X., 2024. Sparse modal decomposition method addressing underdetermined vortex-induced vibration reconstruction problem for marine risers. China Ocean Eng. 38 (2), 285–296.

Duranay, A., Demirhan, A.E., Dobrucali, E., Kinaci, O.K., 2023. A review on vortex-induced vibrations in confined flows. Ocean Eng. 285, 115309.

Esmaeili, M., Rabiee, A.H., 2021. Active feedback VIV control of sprung circular cylinder using TDE-iPID control strategy at moderate Reynolds numbers. Int. J. Mech. Sci. 202, 106515.

Facchinetti, M.L., De Langre, E., Biolley, F., 2004. Coupling of structure and wake oscillators in vortex-induced vibrations. J. Fluid Struct. 19 (2), 123–140.

Fukami, K., Fukagata, K., Taira, K., 2019. Super-resolution reconstruction of turbulent flows with machine learning. J. Fluid Mech. 870, 106–120.

Gao, Y., Fu, S., Ren, T., Xiong, Y., Song, L., 2015. VIV response of a long flexible riser fitted with strakes in uniform and linearly sheared currents. Appl. Ocean Res. 52, 102–114.

Gao, X.F., Xie, W.D., Xu, W.H., Bai, Y.C., Zhu, H.T., 2018. A novel wake oscillator model for vortex-induced vibrations prediction of a cylinder considering the influence of Reynolds number. China Ocean Eng. 32 (2), 132–143.

Huang, K., Chen, H.C., Chen, C.R., 2011. Numerical scheme for riser motion calculation during 3-D VIV simulation. J. Fluid Struct. 27 (7), 947–961.

Jiang, Z., Li, P., Feng, L., Wang, Y., Liu, L., Guo, H., 2021. Experimental investigation on the VIV of two side-by-side risers fitted with triple helical strakes under coupled interference effect. J. Fluid Struct. 101, 103202.

Jiang, K., Xue, S., Xie, L., Wan, G., 2024. A cross-polarized antenna sensor based on U-shaped resonator for crack sensing. Measurement 231, 114592.

Kamilaris, A., Prenafeta-Boldú, F.X., 2018. Deep learning in agriculture: a survey. Comput. Electron. Agric. 147, 70–90.

Karniadakis, G.E., Kevrekidis, I.G., Lu, L., Perdikaris, P., Wang, S., Yang, L., 2021. Physics-informed machine learning. Nat. Rev. Phys. 3 (6), 422–440.

Lake, B.M., Baroni, M., 2023. Human-like systematic generalization through a meta-learning neural network. Nature 623 (7985), 115–121.

Lehn, E., 2003. VIV Suppression Tests on High L/D Flexible Cylinders. Norwegian Marine Technology Research Institute, Trondheim, Norway.
Li, H.N., Ren, L., Jia, Z.G., Yi, T.H., Li, D.S., 2016. State-of-the-art in structural health monitoring of large and complex civil infrastructures. J. Civil Struct. Health Monit. 6, 3–16.
Li, X., Xue, S., Xie, L., Wan, G., 2024. A miniaturized passive wireless patch antenna sensor for structural crack sensing. Struct. Health Monit., 14759217241227797
Lie, H., Kaasen, K.E., 2006. Modal analysis of measurements from a large-scale VIV model test of a riser in linearly sheared flow. J. Fluid Struct. 22 (4), 557–575.
Liu, W., Liang, R., Zhang, H., Wu, Z., Jiang, B., 2023. Deep learning based identification and uncertainty analysis of metro train induced ground-borne vibration. Mech. Syst. Signal Process. 189, 110062.
Liu, D., Ai, S., Sun, L., Soares, C.G., 2024. Vortex-induced vibrations of catenary risers in varied flow angles. Int. J. Mech. Sci. 269, 109086.
Lu, Y., Liao, Y., Liu, B., Xu, W., 2019. Cross-flow vortex-induced vibration reduction of a long flexible cylinder using 3 and 4 control rods with different configurations. Appl. Ocean Res. 91, 101900.
Lu, Y., Liao, Y., Xu, W., 2020. An investigation into the fatigue damage of a long flexible cylinder with multiple control rods in crossflow. Ocean Eng. 202, 107175.
Martini, S., Morgut, M., Pigazzini, R., 2021. Numerical VIV analysis of a single elastically-mounted cylinder: comparison between 2D and 3D URANS simulations. J. Fluid Struct. 104, 103303.
Mukundan, H., Modarres-Sadeghi, Y., Dahl, J.M., Hover, F.S., Triantafyllou, M.S., 2009. Monitoring VIV fatigue damage on marine risers. J. Fluid Struct. 25 (4), 617–628.
Raissi, M., Perdikaris, P., Karniadakis, G.E., 2019. Physics-informed neural networks: a deep learning framework for solving forward and inverse problems involving nonlinear partial differential equations. J. Comput. Phys. 378, 686–707.
Sekar, V., Jiang, Q., Shu, C., Khoo, B.C., 2019. Fast flow field prediction over airfoils using deep learning approach. Phys. Fluids 31 (5).
Sun, H., Büyüköztürk, O., 2015. Optimal sensor placement in structural health monitoring using discrete optimization. Smart Mater. Struct. 24 (12), 125034.
Trim, A.D., Braaten, H., Lie, H., Tognarelli, M.A., 2005. Experimental investigation of vortex-induced vibration of long marine risers. J. Fluid Struct. 21 (3), 335–361.
Wang, E., Xiao, Q., 2016. Numerical simulation of vortex-induced vibration of a vertical riser in uniform and linearly sheared currents. Ocean Eng. 121, 492–515.
Wang, P., Tian, X., Peng, T., Luo, Y., 2018. A review of the state-of-the-art developments in the field monitoring of offshore structures. Ocean Eng. 147, 148–164.
Wang, Y., Zhu, S., Wang, B., Qin, J., Qin, G., 2024. Structural health monitoring of oil and gas pipelines: developments, applications and future directions. Ocean Eng. 308, 118293.
Weber, M., Engert, M., Schaffer, N., Weking, J., Krcmar, H., 2023. Organizational capabilities for ai implementation—coping with inscrutability and data dependency in ai. Inf. Syst. Front. 25 (4), 1549–1569.
Xie, W., Gao, X., Wang, E., Xu, W., Bai, Y., 2019. An investigation of the nonlinear dynamic response of a flexible pipe undergoing vortex-induced vibrations and conveying internal fluid with variable-density. Ocean Eng. 183, 453–468.
Xu, W.H., Yang, M., Ai, H.N., He, M., Li, M.H., 2020. Application of helical strakes for suppressing the flow-induced vibration of two side-by-side long flexible cylinders. China Ocean Eng. 34 (2), 172–184.
Xue, S., Wang, H., Xie, L., Li, X., Zheng, Z., Wan, G., 2024. Bolt loosening detection method based on double-layer slotted circular patch antenna. Struct. Health Monit., 14759217241227992
Zhang, C., Kang, Z., Stoesser, T., Xie, Z., Massie, L., 2020. Experimental investigation on the VIV of a slender body under the combination of uniform flow and top-end surge. Ocean Eng. 216, 108094.
Zhang, J., Huang, B., Zhang, M., Liu, T., Wu, Q., 2024. Investigation of vortex-induced vibration characteristics around the NACA0009 hydrofoil with a focus on the lock-in phenomenon. Ocean Eng. 312, 119082.
Zhu, H., Hu, J., Zhao, H., Gao, Y., 2021. Experimental study on the vortex-induced vibration of a catenary flexible riser under sheared flows. Int. J. Offshore Polar Eng. 31 (3), 283–292.
Zhu, H., Xu, H., Liu, B., Zhong, J., 2024. Numerical investigation of the vortex-induced vibration of a circular cylinder in oscillatory flow. Ocean Eng. 310, 118666.